Sherrington-Kirkpatrick model analysis of fMRI-BOLD data from Alzheimer's patients and healthy controls

Author: Giada Damiani*
Master en Física dels Sistemes Complexos i Biofísica.
Facultat de Física, Universitat de Barcelona, Martí i Franquès 1, 08028 Barcelona, Spain.

Advisors: Giulio Ruffini[1], Demian Levis[2], Jakub Vohryzek[3]
[1]*Neuroelectrics Barcelona, Barcelona, Spain*
[2]*Facultat de Física, Universitat de Barcelona, Martí i Franquès 1, 08028 Barcelona, Spain and*
[3]*Computational Neuroscience Group, Center for Brain and Cognition (Department of Information and Communication Technologies), Universitat Pompeu Fabra, Barcelona, Spain*
(Dated: July 1, 2024)

This thesis aimed to advance the understanding of Alzheimer's disease (AD) using computational modelling tools rooted in statistical physics. Specifically, pseudo-likelihood maximisation of a spin-glass model was employed to extract coupling matrices J from fMRI-BOLD data of elderly subjects diagnosed with AD and healthy controls (HC). Data was sourced from participants in the European Project Neurotwin's clinical trial, where AD patients undergo brain stimulation as a potential treatment, and from the AD Neurological Initiative (ADNI) database for the healthy controls. The derived coupling matrices were then compared between conditions to identify differences in brain connectivity. The research also explored the criticality of these systems using Metropolis simulations to assess phase transitions and critical temperatures. First, the focus was on extracting and analysing the J matrices. It was found that the J homotopic connectivity decreased in the AD subjects compared to the healthy ones with weak statistical significance ($p = 0.0496$), a finding consistent with other studies on inter-hemispheric connectivity disruption in AD. Moreover, the J matrices' standard deviation significantly differed between the HC and AD groups ($p = 0.0039$). Additionally, brain areas with the highest change in J across conditions aligned with regions previously identified in functional connectivity studies of AD. Then, the spin-glass systems — defined by the condition-specific J's — were simulated with the Metropolis algorithm. The critical temperature was found to be lower in the AD spin lattice compared to the HC spin lattice, suggesting that the AD state is closer to a disordered (paramagnetic) phase, which aligns with the hypothesis that weaker inter-parcel connections in AD may lead to a state nearer to the paramagnetic phase transition. The research highlighted the potential of the J coupling matrix to capture structural features and homotopic connections, which can serve as a synthetic brain connectome when dMRI is unavailable. Future work will include using longer data and other type of data (e.g. new healthy controls, and pre- and post-stimulation data), and the optimisation of the sparsity value in the extraction of J. Also, the criticality analysis may be improved by building a theoretical phase diagram based on J characteristics.

I. INTRODUCTION

Alzheimer's disease (AD) is a complex neurodegenerative disorder that impairs cognitive functions [1]. Researchers have extensively studied the disease in genetics, molecular biology, and neuroimaging [2], producing valuable data for understanding the disease and defining its biomarkers [1]. Functional MRI (fMRI) has identified significant changes in brain signals associated with AD. The most common fMRI method is blood oxygenation level-dependent (BOLD) imaging. fMRI-BOLD uses haemoglobin as an endogenous contrast agent, exploiting the magnetisation difference between oxyhemoglobin and deoxyhemoglobin to generate the signal. In other words, fMRI-BOLD measures neuronal activity indirectly through its hemodynamic correlate [3]. Resting-state fMRI-BOLD experiments aim to map functional communication between brain regions by measuring the correlation of fMRI time-series dynamics [4]. This process, known as functional connectivity (FC), refers to the relationship between the neuronal activation patterns of anatomically distinct brain regions, indicating the level of functional communication between them [4]. Numerous studies have shown alterations in resting-state FC in AD. Generally, there is a decrease in FC within the hippocampal [5, 6] and posterior cingulate regions [7, 8]. Conversely, increased FC has been observed between the prefrontal cortex and hippocampus [5], and between the prefrontal and posterior cingulate cortices [7, 8], suggesting a potential compensatory mechanism driven by the prefrontal cortex, particularly in the early stages of AD [9–11].

While fMRI provides insights into functional brain activity, anatomical MRI (aMRI) and diffusion MRI (dMRI) contain information on the brain structure and connections. Both functional and anatomical data types are necessary for computational models, as these models investigate the relationship between structure and function [12]. An aMRI scanner delivers a specific ra-

* gdamiada7@ub.alumnes.edu

dio frequency that excites the hydrogen atoms in water molecules, which return some of this energy as a distinctive nuclear magnetic resonance signal [13]. Therefore, this technique can be used to discover the presence of abnormal tissue through the changes in tissue density or composition, including brain volume loss (atrophy) observed in AD patients [14]. In this thesis, aMRI data was only used for brain parcellation, i.e., assigning each MRI voxel to a brain sub-area. A voxel, short for "volumetric pixel," is the smallest unit of volume in 3D imaging, similar to a pixel in 2D images. It represents data about the tissue within that specific space in MRI scans. dMRI is a technique used to quantify the random motion of water molecules within biological tissues. This motion, influenced by tissue microstructure, can reveal insights into the orientation and integrity of cellular fibres in the brain. By applying gradients of varying directions and strengths to the magnetic field during image acquisition, dMRI generates data that can be analysed to infer the presence and orientation of these fibres, a process known as tractography. Diffusion tensor imaging (DTI) is a specific application of dMRI that models diffusion as a tensor to provide maps of white matter architecture and connectivity [15]. This thesis used dMRI data to provide the brain's physical connections as a reference for the features extracted from fMRI-BOLD data.

Several methods exist to analyse the dynamics in fMRI-BOLD data, including sliding-window functional connectivity analysis, dynamic causal modelling, oscillation analysis, and biophysical modelling. This study explores the potential of a different approach: spin-glass modelling, based on the critical brain hypothesis.

The brain is a complex system which can be analysed with tools from statistical physics [16–24]. Similar to how materials transition between ordered (solid) and disordered (gas) phases, neural networks can switch between synchronised and unsynchronised states. Near phase transitions, or critical points, a balance of order and disorder is maintained, which is considered crucial for living organisms [25]. At the critical point, complex collective patterns emerge, resulting in rich long-range correlations across the system. Here, fluctuations are structured according to fundamental physical principles and symmetries, leading to 'universality classes' of coordinated activity [26].

Theoretical work suggests that computation and information dynamics in complex systems exhibit unique features at critical points [27–31]. Criticality is proposed as a key principle to explain the brain's complexity, allowing it to process diverse information sources and guide behaviour in complex environments [17, 32–38]. Additionally, systems in nature often tune themselves to a critical state, a concept known as 'self-organised criticality' [39–41]. Building on this pioneering work, this thesis uses tools from statistical physics to study brain dynamics that support different states of consciousness, specifically the conditions of AD and healthy.

The aim of this thesis was first to extract features from the fMRI-BOLD time series of Alzheimer's patients and healthy controls using pseudo-likelihood maximisation of a spin-glass model (coupling matrix J and personalised temperatures) and Metropolis simulations of spin systems (criticality metrics). Then, we compared these features by condition and subject. Finally, the coupling matrix J was compared to the fMRI-BOLD-derived functional connectivity and to the physical brain connectome derived from dMRI data.

This thesis is part of the Neurotwin project (neurotwin.eu), which aims to develop brain models for characterising individual pathology, predicting the physiological effects of transcranial electromagnetic stimulation, and designing optimal stimulation protocols for AD. This work contributes by creating macroscale brain models for AD and healthy conditions. Future research will explore whether stimulation can induce changes in the AD model to resemble the healthy model.

For this thesis, I processed the Neurotwin clinical trial data, selected and processed healthy controls (HC) data from the ADNI database [42], maintained, used and developed parts of the software for fMRI-BOLD preprocessing, spin model fitting, and Metropolis simulations. I was also responsible for the analysis and writing. The methods presented here were used in previous work [43] (with some modifications), in which we analysed fMRI-BOLD data from a within-subject study, where the individuals were observed during different sessions under the influence of lysergic acid diethylamide (LSD) or a placebo.

II. METHODS

An overview of the methods used in this thesis is shown in Figure 1.

A. MRI data for Alzheimer's patients and healthy controls

This thesis used two datasets: one for patients diagnosed with Alzheimer's disease (AD) and one for healthy controls (HC). The AD dataset is from an ongoing clinical trial with AD patients part of the European project Neurotwin, and it includes 17 subjects (8 women, mean sample age 72.9 ± 5.5 years old). The trial aims to determine whether brain stimulation can improve patients' conditions and slow down the progression of the neurodegenerative disease. The data used in this thesis is from pre-treatment scans.

Both datasets included data from the imaging modalities fMRI (functional information), dMRI (information on the physical structure of brain connections), and aMRI (anatomical information needed for the preprocessing of the other two modalities). fMRI images were acquired using blood oxygenation level-dependent (BOLD) imaging (repetition time TR = 0.98 s, echo time TE = 30.41 ms, flip angle FA = 63°, slice thickness = 2.8 mm,

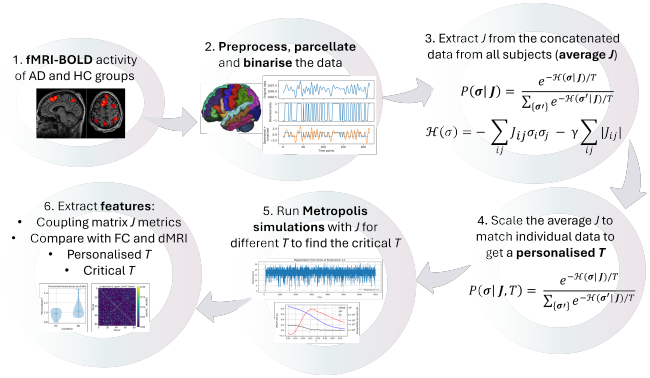

FIG. 1: Methods overview: fMRI-BOLD data from AD and healthy control (HC) conditions (1) was preprocessed, assigned to brain areas and binarised (2). Then, we found the J that best matched the data with pseudo-likelihood maximisation, with system temperature $T = 1$ (3). Then the "average J" was scaled to match individual data using "personalised temperatures" (4). Step 4 was skipped when individual data was directly used in Step 3. Metropolis simulations were run with J at different temperatures to find the critical temperature (5). Condition- and subject-specific features were extracted from J and compared to functional connectivity (FC) and dMRI connectomes. Personalised and critical temperatures were compared across conditions (6).

number of time points = 487, total duration = 8 min). Diffusion Tensor Images (DTI) were acquired using a total of 121 diffusion sampling directions (b-value: b0 x 10, b300 x 8, b1000 x 32, b2500 x 71; TR: 3400 ms; TE: 80 ms; FA: 90°; voxel size: 1.79x1.79 mm; slice thickness: 1.79 mm).

The HC dataset is sourced from the Alzheimer's Disease Neuroimaging Initiative (ADNI) database [42], which includes data from elderly individuals with and without AD. Subject data for 17 healthy elderly individuals (8 women, mean sample age 73.0±5.2 years old) was selected to match the mean age and sex distribution of the AD dataset. The specific acquisition parameters for this data vary by subject and are detailed in Appendix A.

B. Parcellated fMRI-BOLD time series and functional connectivity

The fMRI-BOLD data was preprocessed to remove artefacts (e.g. caused by head motion or fluctuations in the MRI scanner's hardware) and extract the mean fMRI-BOLD activity per brain region (or parcel) at each time point. The preprocessing steps included:

1. Minimal preprocessing of the fMRI-BOLD images using fMRIPrep [44] software, which involved coregistration to the anatomical MRI, application of slice timing correction, and estimation of head motion artefacts.
2. Division of the functional image into 84 brain parcels and registration to a standard coordinate system using Freesurfer [45] and ANTs [46] software, followed by further cleaning to remove the head motion artefacts estimated by fMRIPrep.
3. Extraction of the fMRI-BOLD signal for each brain parcel by averaging the activity of the voxels within each parcel, using in-house code.
4. Application of global signal regression (GSR) to reduce global fluctuations by regressing out the average signal intensity across all brain parcels from each parcel's time series.

The fMRI-BOLD signal is represented as a matrix with dimensions (brain parcel × time slice) for each subject. Brain parcels were defined according to the Desikan84 parcellation scheme [47]. Parcel names and indices are in Appendix B, and the methods used to create the brain atlas can be found in *Desikan et al. (2006)* [47].

The functional connectivity, FC, was computed from the fMRI-BOLD time series as the Pearson correlation between the activity of each pair of parcels across time and is represented as a matrix with dimensions (brain parcel × brain parcel). Pearson correlation is a statistical measure that quantifies the strength and direction of the linear relationship between two continuous variables. It ranges from −1 to 1, where 1 (−1) indicates a perfect positive (negative) linear relationship and 0 indicates no linear relationship. It assumes that the variables are normally distributed and have a linear relationship.

C. Parcellated dMRI connectome

The dMRI data was preprocessed to remove noise and artefacts, e.g. image distortions caused by magnetic field gradients. Using Freesurfer [45] and MRTrix [48], a tractogram was generated based on the Desikan84 parcellation scheme [47]. A tractogram models the three-dimensional pathways of white matter tracts in the brain. For each subject, a dMRI connectome was derived from the tractogram. This connectome, represented as a matrix with dimensions (brain parcel × brain parcel), contains the sum of connections between each pair of parcels.

D. Down-sampling and adjustment of fMRI-BOLD data

Initially, the analysis was conducted using the preprocessed fMRI-BOLD data, as described above. However, we observed significant differences in acquisition parameters between the two fMRI-BOLD datasets. The main parameters that differed between the two datasets were the repetition time and the number of time points. Repetition time refers to the time that passes between consecutive acquired brain volumes. It determines how frequently data are acquired, impacting the scan's temporal

resolution. Number of time points refers to the number of brain volume acquisitions in time. These parameters influence the balance between scan duration and the temporal resolution of the scans.

The AD data had consistent scan parameters across subjects, including repetition time, number of time points, and total duration. In contrast, the HC data had heterogeneous scan parameters, lower temporal resolution and fewer time points than the AD data.

To reduce this technical variability, we adjusted the AD data (and data from a few HC subjects) to match the lowest-resolution scan parameters of the HC data. The adjustments included:

- Increasing the repetition time (time between fMRI-BOLD volume samples in time) of the AD data from 1 s to 3 s, which is the largest repetition time in the HC data.
- Reducing the number of time points in the AD data from 487 to 139, the lowest number of time points in the HC data.

Data was down-sampled using the `decimate` function from the `scipy.signal` module, which reduced the signal's sampling rate while minimising aliasing effects through low-pass filtering, and maintaining zero phase distortion. These adjustments improved comparability between the datasets but also reduced the temporal resolution of the AD data. Finally, two subjects from the HC group were excluded due to preprocessing issues, where excessive image noise led to zero activity in some parcels. After this exclusion, the HC sample contained data from 7 women with a mean sample age of 72.8 ± 5.4 years old.

E. fMRI-BOLD data binarisation

The fMRI-BOLD data was normalised and binarised so it could be modelled with binary Ising spins. For every brain parcel, the median of the time signal was used as a threshold for binarisation. All the values above (below) the median of the signal were assigned to 1 (-1).

F. Spin models

Spin models from statistical physics can describe the emergence of collective phenomena — such as phase transitions — in large systems composite of smaller parts, e.g., spins or brain parcel activity, which interchange information under the assumptions of the maximum entropy principle [49–51]. Complex systems can be analysed through coarse-graining variables describing macrostates. Continuous phase transitions happen at the so-called critical points, where the system macrostate changes qualitatively. Here, observable quantities such as heat capacity, correlation length or susceptibility to external perturbations diverge in the thermodynamic limit, i.e., as the number of spins goes to infinity. At these transitions, from order to disorder, the system is scale-free, with fractal properties in energy and information flow.

In this context, elements such as brain regions are modelled by spins (i.e., with two states, up or down, active or inactive) with pair interactions. The statistical properties of large spins systems are studied under different conditions determined by varying the control parameter, i.e., the temperature. The prototypical simplest system in this context is the classical two-dimensional Ising model, which features nearest-neighbour interactions and a phase transition. Also, the fact the brain exhibits characteristics of criticality that may be modelled by systems such as spin models is now well established, with ideas that go back to pioneers such as Turing [52], Bak [16, 53], and Hopfield [54]. There is further evidence that the dynamics of the healthy brain occupy a sub-critical zone ([55],[56] and references therein).

The spin model used in this thesis is essentially the Sherrington-Kirkpatrick (SK) spin-glass model [57], which was introduced as an extension of the original Ising model in the presence of disordered interactions. The SK model allows for a random J with values specific for each pair of spins, at any distance, i.e., all spins are interconnected with an arbitrary weight, in contrast to the original Ising model, where J is constant with only nearest-neighbour interactions.

The SK model is defined by the energy or Hamiltonian of the lattice of N spins with pairs of parcels i and j (i, $j \in [1, N]$, $i \neq j$), given by

$$\mathcal{H}(\sigma) = -\sum_{i<j} J_{ij}\sigma_i\sigma_j - \sum_i h_i\,\sigma_i - \gamma \sum_{i<j} |J_{ij}| \quad (1)$$

where the sum over $i < j$ denotes a sum over all pairs of spins (with pairs counted once), σ_i denotes the orientation of spin i in the lattice (± 1), J_{ij} is the coupling matrix or Ising connectivity, and h_i is an external magnetic field applied independently at site i. We assume that self-connections are zero ($J_{ii} = 0$) and that J is symmetric ($J_{ij} = J_{ji}$). N.B. The last term was added to the original SK Hamiltonian to force the sparsity of the matrix when extracting J (see subsection II F 1). We use the L1 norm with γ being the sparsity value and $|...|$ denoting the absolute value.

In the context of analysis of parcellated fMRI-BOLD data, σ_i represents the binarised state of each brain parcel and is equal to $+1$ (-1) when the parcel is active (inactive), h_i is a parameter that modulates the mean activity in a single parcel, and $J_{ij} \in \mathbb{R}$ is a parameter that accounts for the interactions between parcels i and j (activity correlations), and which can be positive or negative. Here, $\mathcal{H}$ is not a physical energy but is a mathematical construct which allows to rationalise the frequency (or probability distribution) of finding a given activity pattern σ. If an activity pattern rarely occurs in the data, it will correspond to high energy and vice versa. It is worth noting that in the original SK model, the interactions J_{ij} are independent random variables from the

same distribution defined by its mean and standard deviation. In contrast, in this work, J_{ij} was inferred from the data (see subsection II F 1). From this point forward, we set $h = 0$ in the Hamiltonian, as the h term did not reveal any significant system properties or affect the results.

An essential point in the context of spin models is that there is a competition between the tendency to order and disorder, or in other words, between the spin-spin interactions (determined by the coupling matrix J, which gives the system structure and order) and the thermal agitation that drives the system towards disorder. At low temperatures, spin-spin interactions will prevail, whereas thermal agitation will prevail at high temperatures.

The so-called order parameter is used to evaluate the system macrostate, i.e., in which phase the system happens to be. In the two-dimensional Ising model, it is common to use the magnetisation (average net spin alignment) as the order parameter. In the paramagnetic phase (disordered, no correlation between spin alignment), the magnetisation is zero, whereas in the ferromagnetic phase (ordered, all spins aligned), this is different than zero, as shown in Figure 2.

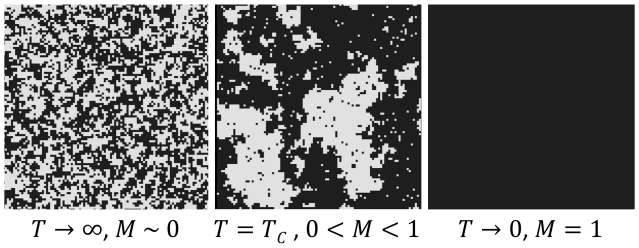

FIG. 2: As the system temperature T is decreased, the magnetisation M abruptly changes from 0 (paramagnetic phase) to 1 (ferromagnetic phase) at the critical temperature T_C.

On the other hand, a spin-glass allows for transitions between three different phases: ferromagnetic (spin overlap > 0, magnetisation different than 0), paramagnetic (spin overlap $= 0$, magnetisation $= 0$), spin-glass (spin overlap > 0, magnetisation $= 0$) [58]. The spin overlap is the average equilibrium configuration obtained from the equilibrium configurations of different realisations of a spin lattice with the same bonds (more details in the subsection II F 5) [58].

1. *Maximum entropy principle derivation of spin models*

Spin models can be derived using the Maximum Entropy Principle (MEP) [49], which finds the most suitable probability distribution given certain constraints, such as data-derived spin correlation values. According to the MEP, the optimal probability distribution maximises entropy while obeying these constraints. The probability of observing a specific spin configuration $\boldsymbol{\sigma}$ in thermal equilibrium at temperature T is given by the Boltzmann distribution [20]:

$$P(\boldsymbol{\sigma}, T|\boldsymbol{J}) = \frac{e^{-\mathcal{H}(\boldsymbol{\sigma}|\boldsymbol{J})/K_B T}}{\sum_{\{\boldsymbol{\sigma'}\}} e^{-\mathcal{H}(\boldsymbol{\sigma'}|\boldsymbol{J})/K_B T}} \tag{2}$$

where K_B is the Boltzmann constant, which will be set to 1 from here onwards to simplify notation, and since we do not deal with physical temperatures. Also, $T = 1$ without loss of generality, $\mathcal{H}$ is defined in Equation 1, and $\sum_{\{\boldsymbol{\sigma'}\}}$ is a sum over all the 2^N possible spin configurations.

2. *Estimation of the coupling matrix J using maximum pseudo-likelihood*

We estimate the coupling matrix J using an approximation to maximum likelihood as described in *Ezaki et al. (2017)* [20]. Briefly, we find the J that maximises the probability of observing the data given the model,

$$\boldsymbol{J} = \arg\max_{\boldsymbol{J}} \mathcal{L}(\boldsymbol{J}) = \arg\max_{\boldsymbol{J}} \log \mathcal{L}(\boldsymbol{J}) \tag{3}$$

where $\mathcal{L}(\boldsymbol{J})$ is defined as

$$\mathcal{L}(\boldsymbol{J}) = \prod_{t=1}^{t_{\max}} P(\boldsymbol{\sigma}(t)|\boldsymbol{J}) \tag{4}$$

where $P(\boldsymbol{\sigma}(t)|\boldsymbol{J})$ is the Boltzmann distribution of the σ pattern at a specific time point t, and t_{max} is the maximum time point. The likelihood maximum can be found by gradient ascent, with

$$J_{ij}^{\text{new}} = J_{ij}^{\text{old}} + \eta \left(\langle \sigma_i \sigma_j \rangle_{\text{empirical}} - \langle \sigma_i \sigma_j \rangle_{\text{model}} \right) \tag{5}$$

where the old/new superscripts refer to the values before and after updating, and with η a small positive constant, which represents the mean error between the old and new J. In Equation 3, we use $\log \mathcal{L}(\boldsymbol{J})$ since the function maximum value is the same as the one of the original, but allows us to have sums instead of products, which is more convenient for gradient ascent.

When the number of spins in the system is very large, calculating the likelihood from the model is computationally expensive. For this reason, we use an approximation known as the pseudo-likelihood, a mean-field approximation that approaches the true likelihood as the number of time points, t, approaches infinity [20, 59],

$$\mathcal{L}(\boldsymbol{J}) = \prod_{t=1}^{t_{\max}} P(\boldsymbol{\sigma}(t)|\boldsymbol{J}) \approx \prod_{t=1}^{t_{\max}} \prod_{i=1}^{N} \tilde{P}(\sigma_i(t)|\boldsymbol{J}, \boldsymbol{\sigma}_{/i}(t)) \tag{6}$$

where $\tilde{P}(\sigma_i|\boldsymbol{J}, \boldsymbol{\sigma}_{/i})$ is the modelled probability distribution for a specific spin given the states of all the others, a quantity much easier to compute, defined as

$$\tilde{P}(\sigma_i|\boldsymbol{J}, \boldsymbol{\sigma}_{/i}) = \frac{e^{-\mathcal{H}_i(\boldsymbol{\sigma}|\boldsymbol{J})}}{\sum_{\sigma_i'} e^{-\mathcal{H}_i(\sigma_i'|\boldsymbol{J}, \boldsymbol{\sigma}_{/i})}} \tag{7}$$

with $\mathcal{H}_i(\boldsymbol{\sigma}|\boldsymbol{J})$ from Equation 1.

Using this approximation, the gradient ascent rule becomes

$$J_{ij}^{\text{new}} = J_{ij}^{\text{old}} + \eta \left(\langle \sigma_i \sigma_j \rangle_{\text{empirical}} - \langle \sigma_i \sigma_j \rangle_{\tilde{P}} \right) \tag{8}$$

where $\langle \sigma_i \sigma_j \rangle_{\tilde{P}}$ is the two-point correlation function with respect to distribution $\tilde{P}$ [20],

$$\langle \sigma_i \sigma_j \rangle_{\tilde{P}} = \frac{1}{t_{\max}} \sum_{t=1}^{t_{\max}} \sigma_j(t) \tanh \left(\sum_{\substack{j'=1 \\ j' \neq i}}^{N} J_{ij'} \sigma_{j'}(t) \right) \tag{9}$$

Coupling matrices J were generated for every participant, from their individual binarised fMRI-BOLD data. A global coupling matrix J was estimated based on concatenated data from all the participants. We similarly derived condition-specific coupling matrices J based on concatenated data for the AD and HC conditions, separately.

3. *Personalisation of model with individual temperatures*

When a global coupling matrix J is generated using the entire dataset, we adapt J for each subject and condition by changing the model temperature $T = 1/\beta$, that is, by writing

$$P(\boldsymbol{\sigma}|\boldsymbol{J}, \beta) = \frac{e^{-\beta \mathcal{H}(\boldsymbol{\sigma}|\boldsymbol{J})}}{\sum_{\{\boldsymbol{\sigma'}\}} e^{-\beta \mathcal{H}(\boldsymbol{\sigma'}|\boldsymbol{J})}} \tag{10}$$

In this case, the gradient ascent algorithm becomes

$$\beta^{\text{new}} = \beta^{\text{old}} - \eta \left(\langle \mathcal{H} \rangle_{\text{empirical}} - \langle \mathcal{H} \rangle_{\tilde{P}} \right) \tag{11}$$

with a fixed point at $\langle \mathcal{H} \rangle_{\text{empirical}} = \langle \mathcal{H} \rangle_{\tilde{P}}$. This, as in the prior equations, can be seen by taking the derivative of the approximate log-likelihood

$$\begin{aligned} \log L(\boldsymbol{J}) &= \sum_{t=1}^{t_{\max}} \log P(\boldsymbol{\sigma}(t)|\boldsymbol{J}) \\ &= \sum_{t=1}^{t_{\max}} \left(-\beta \mathcal{H}(\boldsymbol{\sigma}(t)|\boldsymbol{J}) - \log Z(\boldsymbol{J}, \boldsymbol{\sigma}_{/i}(t), \beta) \right) \end{aligned} \tag{12}$$

with respect to the inverse temperature β, with the partition function, $Z(\boldsymbol{J}, \beta, t) = \sum_{\sigma_i'} e^{-\beta \mathcal{H}_i(\sigma_i'|\boldsymbol{J}, \boldsymbol{\sigma}_{/i}(t))}$.

The first term becomes the average of the empirical Hamiltonian, while the second term is the average model energy. This can be computed from Equation 9 and from

$$\langle \mathcal{H} \rangle_{\tilde{P}} = -\sum_{i<j} J_{ij} \langle \sigma_i \sigma_j \rangle_{\tilde{P}} \tag{13}$$

4. *Analysis of coupling matrix J*

Once the coupling matrix J is found, we can extract several features, such as the mean connectivity, evaluated over the whole network, only the intra-hemispheric (within the same hemisphere), inter-hemispheric (between the two hemispheres), and homotopic network (the same areas in the two hemispheres – mirror areas). Then we can also analyse the absolute value of the connections or only the positive/negative portions. It is interesting to compare the coupling matrix to the raw and binary functional connectivity (obtained from the correlations of the fMRI-BOLD activity between parcels), and to the dMRI-derived connectome with the number of physical connections between pairs of parcels. The former captures the functional properties of the brain, whereas the latter captures the brain's structure. When J is determined separately for the AD and HC groups/subjects, this allows for comparison of these features across conditions.

5. *Metropolis algorithm and spin model features*

The coupling matrix J can be used in Monte Carlo simulations with the Metropolis algorithm to generate synthetic data. This allows us to determine the phase space position for each subject or condition (characterised by their specific J), observe potential phase transitions by varying the temperature, and identify the system's critical point.

In the Metropolis algorithm, a random spin is chosen and flipped with a probability $p = \min(1, \exp[-\Delta\mathcal{H}/T])$, where $\Delta\mathcal{H}$ is the change in energy caused by the flip, and T is the system temperature. In other words, when the spin flip causes the system to go to a state with lower energy, the spin flip is accepted ($p = 1$). On the other hand, when this causes the system to go to a state with higher energy, the flip depends on how the Boltzmann factor compares to a uniform random number between 0 and 1. This process samples the system's probability distribution at a given temperature. If the temperature is high, it is more likely that the spin flip will be accepted. The algorithm is iterated sufficiently to reach a steady state, and macroscopic variables are averaged over many steady-state configurations. To evaluate $\Delta\mathcal{H}$, we express the system's energy (Hamiltonian) as:

$$\mathcal{H}(\sigma) = -\frac{1}{2} \sum_{i,j} J_{ij} \sigma_i \sigma_j \tag{14}$$

$$= -\frac{1}{2} \sum_{i \neq k} \sum_{j \neq k} J_{ij} \sigma_i \sigma_j - \sum_i J_{ik} \sigma_i \sigma_k \tag{15}$$

In the second line, the contribution from spin σ_k is separated out. The energy associated with the k-th spin is $E_i = -\sigma_k \sum_i J_{ik} \sigma_i$. After flipping this spin, its energy contribution becomes $E_f = \sigma_k \sum_i J_{ik} \sigma_i$. Thus, the

energy change ΔE is:

$$\Delta E = E_f - E_i = 2\sigma_k \sum_i J_{ik}\sigma_i \tag{16}$$

The main global observables are the average magnetisation and the spin overlap. The average magnetisation M over the spin lattice of N spin configurations σ_i is computed as

$$M = \frac{1}{N}\sum_{i=1}^{N}\sigma_i \tag{17}$$

and the spin overlap, q, is defined as [58]

$$q = \frac{1}{N}\sum_i S_i^{(k)} \tag{18}$$

where $S_i^{(k)}$ is the equilibrium spin configuration (of spin i) from copy k of the system. The magnetic susceptibility χ and heat capacity C_v are computed by applying a uniform external field h_{ext}:

$$\mathcal{H}(\sigma, h_{ext}) = -\sum_{i<j} J_{ij}\sigma_i\sigma_j - h_{ext}\sum_j \sigma_j \tag{19}$$

The partition function Z is given by:

$$Z(\beta, h_{ext}) = \sum_\sigma e^{-\beta\mathcal{H}(\sigma, h_{ext})} \tag{20}$$

The average magnetisation $\langle M\rangle$ is:

$$\langle M\rangle = \frac{1}{Z}\sum_\sigma M e^{-\beta\mathcal{H}(\sigma, h_{ext})} \tag{21}$$

It can be shown that [60]:

$$\langle M\rangle = \frac{1}{\beta Z}\frac{\partial Z}{\partial h_{ext}} \tag{22}$$

The global susceptibility χ and heat capacity C_v are:

$$\chi = \left.\frac{\partial\langle M\rangle}{\partial h_{ext}}\right|_T = \frac{\sigma_M^2}{T}, \quad C_v = \left.\frac{\partial\langle\mathcal{H}\rangle}{\partial T}\right|_{h_{ext}} = \frac{\sigma_{\mathcal{H}}^2}{T^2} \tag{23}$$

where σ_M^2 and $\sigma_{\mathcal{H}}^2$ are respectively the variances in the magnetisation and energy.

The global susceptibility measures the sensitivity of the lattice state (represented by the magnetisation) to uniform perturbations.

When computing quantities in Metropolis simulations, fluctuations of the order of $1/\sqrt{N}$ are expected. When evaluating magnetisation and global susceptibility, we use $M \to |M| = M\,\mathrm{sign}(M)$, which helps smooth results near the critical point [61]. To ensure steady measurements, we average quantities after discarding the first 10^5 steps to exclude transients, and each simulation runs for over 10^6 Monte Carlo steps, with each step representing a single spin flip. At low temperatures, the acceptance rate of spin flips is very low, causing the lattice to evolve slowly. To mitigate these long equilibration times, the lattice is initialised in an ordered state, i.e., all spins pointing up. While each simulation starts from the same initial conditions, stochasticity comes from how spins are flipped in the Metropolis algorithm, as described above.

Due to a more complex energy landscape, simulations for spin-glasses are more complex than for the classical Ising model. The system can get stuck in local minima and may never escape to reach the global minimum, i.e., it may never overcome the necessary energy barrier to get to the global minimum of the system.

To address this, several approaches can be used:

- **Parallel tempering**: Simulate the system at different temperatures in parallel. Then, after a certain number of iterations, swap configurations (i.e. change the spin states obtained for one temperature with the spin configuration obtained for another temperature) [62].

- **Spin overlap and replicas of the system**:
  - Start from the same initial configuration (all spins pointing up) for quicker convergence to equilibrium at low temperatures. At low temperatures, the system resists change, and the J coupling between parcels mainly determines the final configuration. Starting from an ordered state saves time compared to starting from a disordered state.
  - Average quantities from each simulation, such as magnetisation, susceptibility, energy, and heat capacity.
  - Compute spin overlap (average spin configuration at equilibrium over different replicas).

Parallel tempering was not implemented due to time constraints but will be explored in future work.

Once we find the critical temperature for each subject or condition (from averaging group data), we can compare the critical temperatures across conditions. A higher critical temperature means the system enters a more disordered state or phase at a higher temperature and, therefore, requires a higher temperature to disrupt its structure, determined by the coupling matrix J.

III. RESULTS

A coupling matrix J was determined for each subject individually, from the data of each condition group and all of the data.

Initially, data with the original fMRI-BOLD acquisition parameters was used (subsection III A). Then, the AD data (and part of the HC data) was down-sampled and truncated to match the highest repetition time and lowest number of time points in the HC data, ensuring better comparability of the results (subsection III B). The

analysis was repeated with the down-sampled and truncated data (subsection III C). Since this individual data was quite short, average AD and HC J coupling matrices were built by concatenating all data by condition (subsection III D).

The results show many symmetric matrices with dimensions (parcel × parcel). Due to the order of the brain parcels, detailed in Appendix B, the matrices' upper triangle can be read as shown in Figure 3. The lower triangle is the same but mirrored across the main diagonal. Also, since the matrices are symmetric, we often show the coupling matrix J on the upper triangle of the matrix, and another feature on the lower triangle.

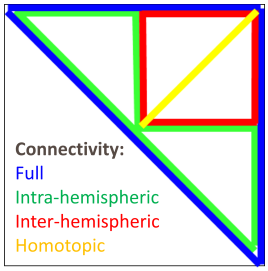

FIG. 3: Guide to interpret matrix plots: full connectivity in blue (outer triangle), intra-hemispheric in green (smaller triangles on diagonal), inter-hemispheric in red (top right square), and homotopic in yellow (square diagonal).

A. Personalised coupling matrix J from data with original acquisition parameters

The J coupling matrix was extracted from individual subject data, specifically with the original fMRI-BOLD acquisition parameters. Here, we used a sparsity value of 0.1, a time step of 0.025, and a maximum number of gradient ascent iterations of 4000 (Equation 8). The J coupling matrices (upper triangle) and the binarised functional connectivity (FC) matrices (lower triangle) are shown for all subjects in Appendix C (Figures 21 and 20), and the mean μ and standard deviation σ_{std} values of the J matrices are shown in Figure 4. Their difference was statistically different (respectively $p = 0.009$ and $p = 7.7 \times 10^{-9}$) due to the different acquisition parameters across condition. Here, we show an example for two subjects, one from each condition, in Figure 5. The AD matrix is more sparse than the HC one (both for J and the binarised FC), and this was consistent across all subjects (Figure 21 and 20). The J coupling matrices were compared to the individual dMRI connectomes, as shown in Figure 6. The dMRI connectome indicates the number of connections between pairs of parcels, hence it only contains positive values. For comparability, the absolute value of J was plotted, and both triangles were divided by their respective maximum values (here, the highest maximum of J and of the connectome between the two subjects). The AD J coupling matrix reconstructs to some degree the intra-hemispheric connections shown in

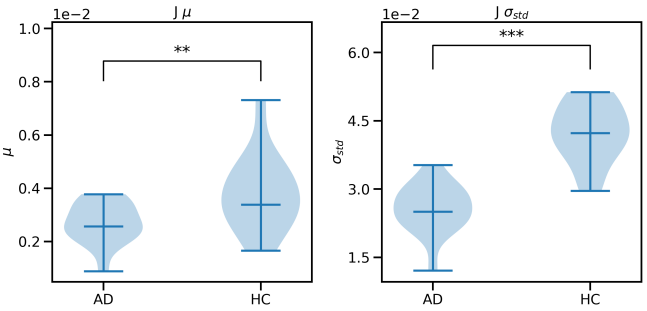

FIG. 4: Mean and standard deviation of non-zero elements of J coupling matrices for AD and HC groups (original data) (** for $p < 0.01$, and *** for $p < 0.001$).

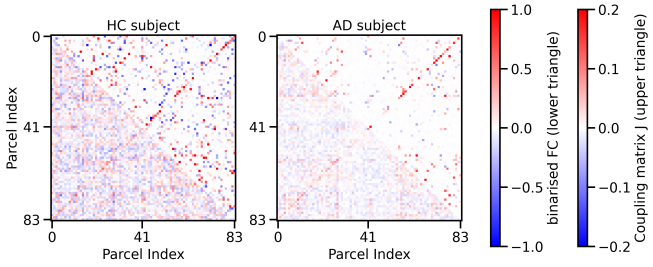

FIG. 5: J coupling matrices (upper triangle) and binarised FC (lower triangle) for two subjects from the HC (left) and AD (right) conditions (original data).

the dMRI connectome, however it also has strong homotopic and some inter-hemispheric connections which are not captured in the connectome, as these come mainly from functional data. The correlation between the J

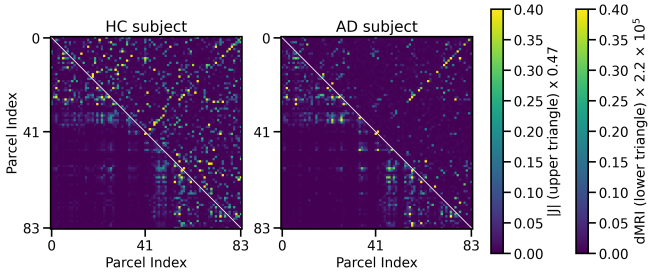

FIG. 6: Comparison between J in absolute value (upper triangle) and dMRI connectome (lower triangle) for an HC patient (left) and an AD subject (right), with original data.

coupling matrices and, respectively, the binarised FC, raw FC (FC before data binarisation), and dMRI connectome are shown in Figure 7, divided by condition. As expected, the correlation with the binarised FC was the highest since it was used for extracting J, followed by the raw FC and the dMRI connectome. The violin plots show the AD distribution in blue (left) and the HC one in orange (right). The two distributions seem quite different, especially for the binarised FC and dMRI connectome.

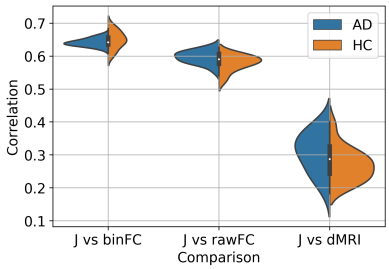

FIG. 7: Correlation between J and binarised/raw functional connectivity and dMRI, divided by condition with AD in blue (left) and HC in orange (right) (original data).

B. Down-sampling and cut

Since both the binarised FC and J coupling matrices for the two condition groups were visibly different (Figures 20 and 21), we down-sampled and truncated the data to match the HC data, to ensure better comparability. The data used here was adjusted to have a repetition time of 3 s and 139 time points (respectively the highest repetition time and lowest number of time points in the HC data). The top plot shows the fMRI-BOLD time signal in a parcel. The original signal (grey) was down-sampled by a factor of 3 and cut. The plot shows the final down-sampled and cut signal in green, where its actual points (circles) were interpolated to be displayed on the original signal. The bottom plot shows the signal in the frequency domain. As expected, the Fourier transform (FT) amplitude was reduced for all frequencies, and the original spectrum shape was preserved.

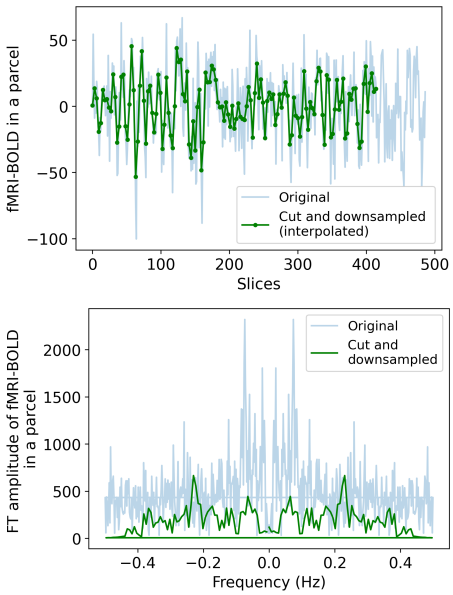

FIG. 8: fMRI-BOLD signal of an AD patient after down-sampling and truncation, in the time (top) and frequency (bottom) domains. FT: Fourier transform.

C. Personalised coupling matrix J from down-sampled data

The J coupling matrix was extracted from individual subject data, which now has the same fMRI-BOLD acquisition parameters for the whole data. For the J extraction, we used a sparsity value of 0.1, a time step of 0.025, and a maximum number of iterations of 4000. The J coupling matrices (upper triangle) and the binarised FC matrices (lower triangle) are shown for all subjects in Figures 23 and 22 (Appendix D). Here, we show an example for two subjects, one from each condition, in Figure 10. After down-sampling, the AD matrix is less sparse and more similar to the HC one. This was consistent across all subjects (Figures 23 and 22). Figure 9 shows that the differences between the mean μ and standard deviations σ_{std} of the J matrices decreased, as expected with the downsampling. However, the σ_{std} still show a statistically significant difference ($p = 0.0039$), possibly due to condition, since the data comparability was improved.

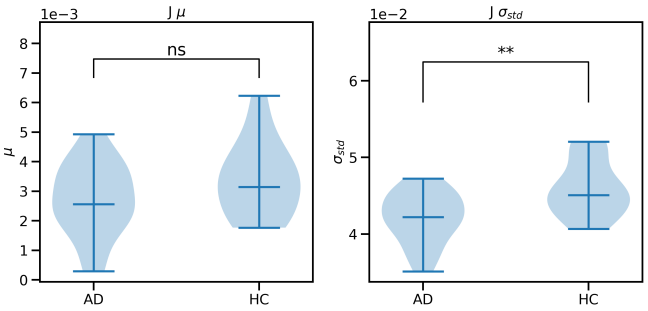

FIG. 9: Mean and standard deviation of non-zero elements of J coupling matrices for AD and HC groups (down-sampled data) (** for $p < 0.01$, and 'ns' indicates a non-significant result, $p \geq 0.05$).

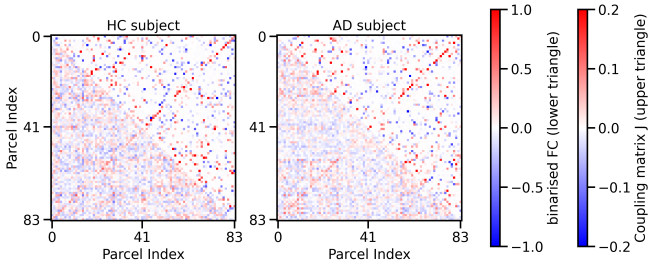

FIG. 10: J coupling matrices (upper triangle) and binarised FC (lower triangle) for two subjects from the HC (left) and AD (right) conditions (down-sampled data).

The J coupling matrices in absolute value (upper triangle) were compared to the individual dMRI connectomes (lower triangle), as shown in Figure 11 for one healthy subject (left) and one AD subject (right). For visualisation purposes, the J matrix was scaled with respect to

the highest maximum from the J's of the two subjects, and same for the dMRI connectome. The correlation

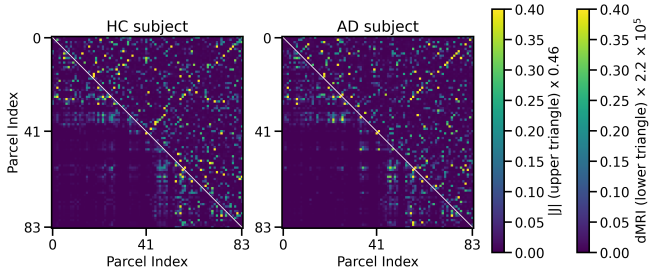

FIG. 11: Comparison between J in absolute value (upper triangle) and dMRI connectome (lower triangle) for an HC patient (left) and an AD subject (right), with original data.

between the J coupling matrices and, respectively, the binarised FC, raw FC, and dMRI connectome are shown in Figure 12, divided by condition. The correlation between J and the binarised and raw FC did not vary much compared to the one in Figure 7, as all three quantities were computed on the same down-sampled and cut data. The correlation with the dMRI connectome is lower here, especially for the AD group, than with the original data (Figure 6). This is expected as the J matrices are now less sparse.

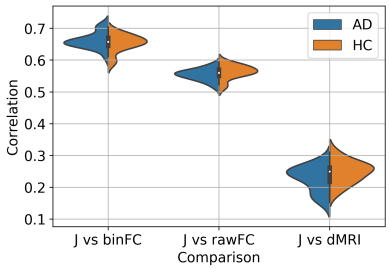

FIG. 12: Correlation between J and binarised/raw functional connectivity and dMRI, divided by condition with AD in blue (left) and HC in orange (right) (original data).

Since comparability between the J coupling matrices was improved, we compared J statistics, such as the mean connectivity in the whole network, in the intra-hemispheric, inter-hemispheric and homotopic networks, and the proportion of negative connections in the same networks, across conditions.

The only weakly significant difference was in homotopic connections ($p = 0.0496$), which decreased in AD. Inter-hemispheric connectivity decreased in AD ($p = 0.09$), and a higher percentage of negative inter-hemispheric connections was observed in AD ($p = 0.13$). The mean connectivity of J, the latter divided by its standard deviation, and the mean intra-hemispheric connections were lower in AD but not significantly (respectively $p = 0.13$, $p = 0.27$ and $p = 0.68$). Also, the percentage of negative connections in the whole J ($p = 0.26$), intra-hemispheric ($p = 0.93$), and homotopic ($p = 0.20$) connections does not differ significantly by condition.

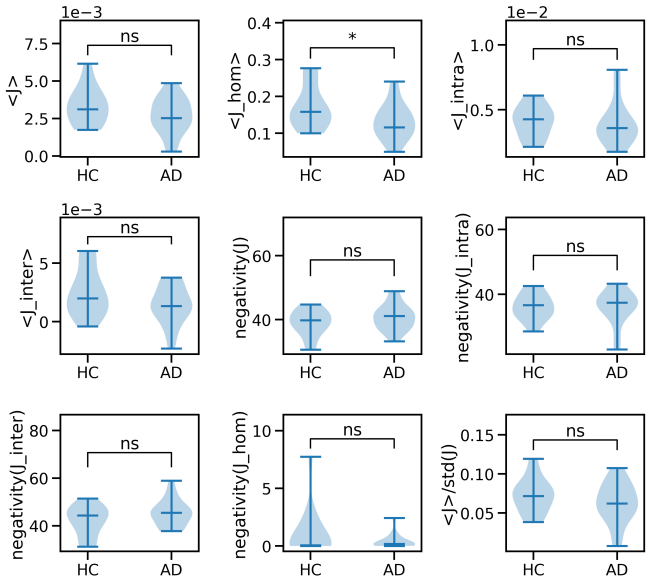

FIG. 13: Comparison between J statistics of AD and HC subjects, from top left to bottom right: mean connectivity of J: full (scaled by 10^{-3}), homotopic, intra-hemispheric (scaled by 10^{-2}), inter-hemispheric (scaled by 10^{-3}); percentage of negative connections in J: full, intra-hemispheric, inter-hemispheric, homotopic. Mean connectivity of J divided by its standard deviation. (* for $p < 0.05$, 'ns' indicates a non-significant result, $p \geq 0.05$).

D. Average coupling matrix J from concatenated down-sampled data

The results from the previous section revealed some interesting trends. However, they were obtained from short individual data (only 139 time points). For the pseudo-likelihood approximation to be valid, longer data is needed. For this reason, we combined all of the down-sampled data to build an average J and combined data from each condition to build average AD and HC J matrices. The off-diagonal elements of the coupling matrices J had the following means $\mu(J)$ and standard deviations $\sigma_{std}(J)$ (here for $T = 1$): for all data, $\mu(J) = 4.6 \times 10^{-3}$ and $\sigma_{std}(J) = 2.9 \times 10^{-2}$; for the HC group, $\mu(J) = 4.9 \times 10^{-3}$ and $\sigma_{std}(J) = 3.1 \times 10^{-2}$; and for the AD group, $\mu(J) = 4.3 \times 10^{-3}$ and $\sigma_{std}(J) = 2.8 \times 10^{-2}$. Their distributions are shown in Figure 14 and are quite similar across conditions: all centred at zero with few negative values and with tails up to 0.05. Figure 15 shows the J coupling matrices and binarised FC for an average model of all of the data (left), only HC (centre) and AD (right). The fit parameters were the same as in the previous simulations. The Pearson correlation coefficients between the J coupling matrices and the binarised FC for all data, HC and AD were 0.63, 0.63 and 0.63 respectively.

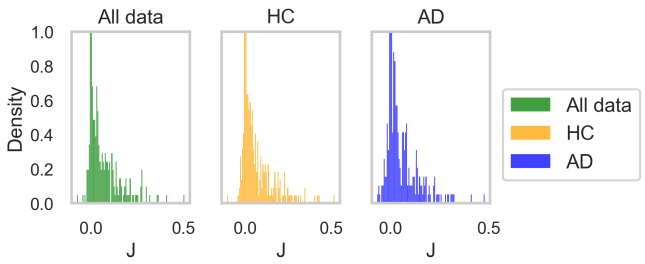

FIG. 14: Histograms of J extracted from all the data (left), HC (middle) and AD (right) data, with a zoom on the less frequent values (Density$_{max} = 1$).

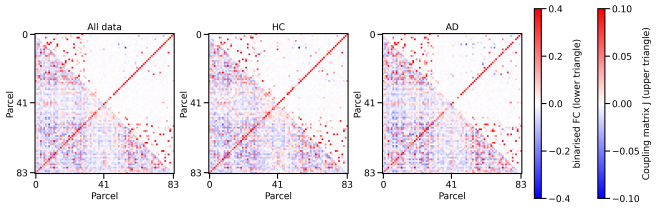

FIG. 15: J coupling matrices (upper triangle) and binarised FC (lower triangle) for an average model of all of the data (left), only HC (centre) and AD (right).

Figure 16 shows the difference between HC and AD in the J coupling matrices and binarised FC. Figures 24 and 25 in Appendix E show the relative difference in respectively J and the binarised FC from HC to AD. Parcels with a change higher than 70% of maximum change (in absolute value) were highlighted and labelled.

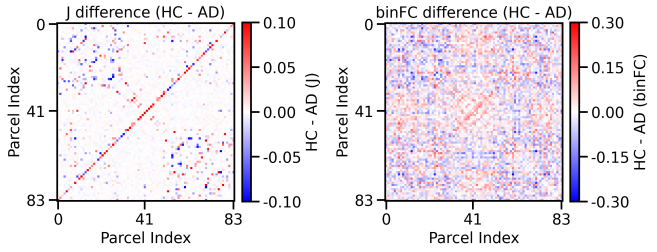

FIG. 16: Difference HC - AD in J coupling matrices (left) and binarised FC (right).

The Pearson correlation coefficients between the delta J coupling matrices and the delta binarised FC (HC - AD) are 0.38 (original matrices), 0.41 (absolute value), 0.50 (positive part) and 0.34 (negative part). The largest changes (HC - AD) in J connection strength between parcels are presented in Table I.

Statistics from the HC and AD J coupling matrices and binarised FC were computed, and their differences are shown in Figure 17 (left). All percentage relative differences were calculated with respect to the value in HC. The mean of J was 11.7% higher in HC than in AD. The J homotopic and inter-hemispheric connections were 21.2% and 22.7% stronger in HC than in AD, respectively. In the AD J matrix, there were more negative connections in the entire matrix (16.5% more than in HC), as well as in the inter- (27.6%) and intra-hemispheric (4.9%) portions. The change in J from HC to AD was negligible for the ratio of mean to standard deviation (1.2%) and for the intra-hemispheric connections (0.3%). The difference between the HC and AD binarised FC was positive for the mean of the whole matrix (92.6%, and 92.8% when divided by the standard deviation) and for the homotopic connections (11.5%). The mean inter- and intra-hemispheric connections were higher in AD by 21.7% and 86.0%, respectively. The difference in the percentage of negative connections from HC to AD was small for the whole matrix (1.3% higher in HC), and for the inter- (1.6% higher in AD) and intra-hemispheric connections (4.4% higher in HC). The results between J and the binarised FC agree (in sign) only on the difference between their means and in the homotopic connections.

Parcel connection	ΔJ
LH Entorhinal - RH Entorhinal	0.17
LH Lingual - RH Lingual	0.15
LH Middle Temporal - LH Superior Temporal	0.13
LH Posterior Cingulate - RH Posterior Cingulate	0.12
LH Precuneus - RH Precuneus	0.13
LH Rostral Middle Frontal - LH Superior Frontal	-0.14
LH Frontal Pole - RH Frontal Pole	-0.17
LH Insula - RH Insula	0.15
LH Thalamus - RH Thalamus	0.15
LH Hippocampus - RH Hippocampus	0.13
LH Amygdala - RH Amygdala	0.12
LH Cerebellum - RH Cerebellum	0.13
RH Middle Temporal - RH Superior Temporal	0.14
RH Inferior Temporal - RH Middle Temporal	0.16

TABLE I: Parcel links with $|\Delta J| \geq 0.12$ (70% of max ΔJ)

Figure 17 also shows the personalised temperatures (right), which were obtained by scaling the average J (from all of the data) to match the individual subject data (see Methods subsection II F 3). There is no statistically significant difference in personalised temperatures between the AD and HC groups ($p = 0.30$).

The absolute values of the J coupling matrices were compared to the dMRI connectomes, which were averaged over the same datasets used for extracting the J matrices (Figure 18). The Pearson correlation coefficients were found to be 0.38 for all data, 0.37 for HC, 0.36 for AD, and 0.28 for the difference between HC and AD.

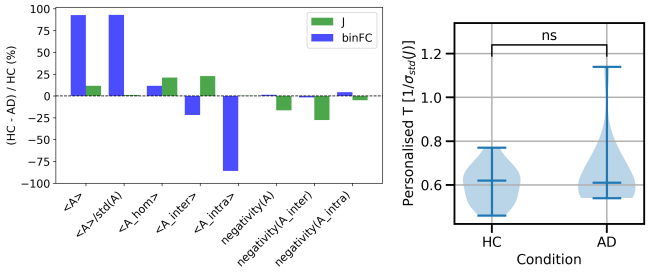

FIG. 17: Left: Difference in metrics obtained from J (green) and the binarised FC (blue) from HC to AD. Labels from left to right: mean of A (either J or binarised FC), mean of A divided by its standard deviation, mean of homotopic, inter-hemispheric and intra-hemispheric part of A, portion of negative connections in A, and its inter- and intra-hemispheric parts. Right: Personalised subject temperatures for the AD and HC groups. $\sigma_{std}(J)$: standard deviation of average J from all data, ns: non-significant p-value.

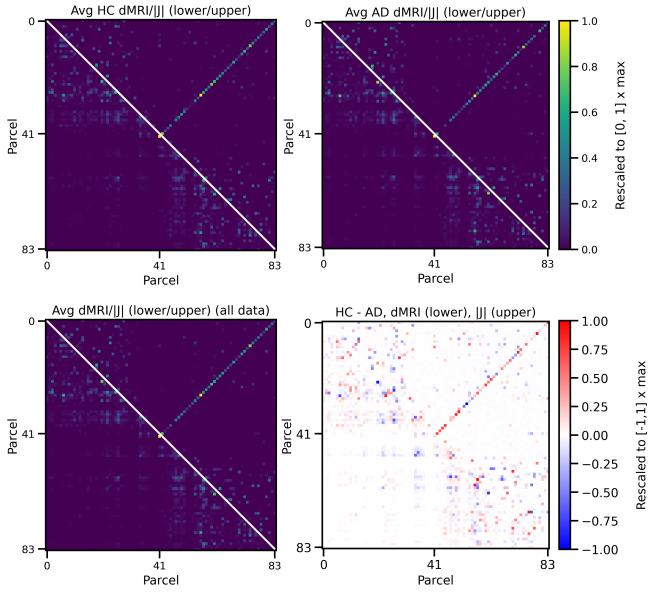

FIG. 18: Comparison between the J coupling matrix in absolute value (upper triangle) and the dMRI connectome (lower triangle) for HC (top left), AD (top right), all data (bottom left) and the difference HC-AD (bottom right). The latter was computed as the difference of the absolute value of the HC J and AD J, since the dMRI connectome only contains positive values. The dMRI connectomes were scaled with respect to the maximum value of the three matrices (2.4×10^5). The same was applied to the J matrices, where the maximum value was 0.52, and the difference matrices. The maximum difference values in J and dMRI were respectively 0.17 and 5.5×10^4.

E. Metropolis simulations with average coupling matrix J from concatenated down-sampled data

First, the code for the Metropolis simulations was validated for a homogeneous $J = 1$ and with nearest-neighbour interactions as it reproduced the results of the classical Ising model in a square lattice.

Then, Metropolis simulations were run for each average J (from all data, HC and AD). For each J, we ran 10 independent realisations, where each realisation had the same parameters, but different random noise (e.g. which spin was randomly selected, or with what random probability the spin flip was accepted or not with a positive energy change).

Figure 19 shows the average magnetisation $\langle M \rangle$, susceptibility $\langle \chi \rangle / N$ and spin overlap q obtained in Metropolis simulations with J from all the data (top) and each condition (middle and bottom), as functions of temperature T. Each point of $\langle M \rangle$ and $\langle \chi \rangle / N$ is the average value of the equilibrium M and χ obtained for each realisation, with Equations 17 and 23. For each realisation, the spin system was simulated for 31 temperatures (from 0.05 to 0.2 in steps of 0.005). The simulations were run for 10^8 steps and the average quantities (M and χ) were computed excluding the first 10^5 steps. Equilibrium was assessed by plotting the magnetisation as a function of time. The dynamics failed to converge to a stable equilibrium value close to the critical point. However, this was mitigated by having multiple copies of the same system. The average equilibrium configuration of spins was extracted from each realisation for each T and brain parcel to compute the spin overlap. Then, the spin overlap was calculated using Equation 18. The plot shows the average data points as circles and the interpolated data as lines. The interpolation was performed using the Savitzky-Golay filter, which smooths the data by fitting a polynomial (here of order 6) to successive subsets of the dataset. The error bars for $\langle M \rangle$ and $\langle \chi \rangle / N$ were computed from the standard deviation of the average magnetisation and susceptibility from each realisation. It is worth noting that the susceptibility error bars near the critical temperature were very large, as the phase transition was happening at slightly different critical temperatures for each realisation. Both the magnetisation and the spin overlap go from a non-zero value to zero, suggesting a phase transition from the ferromagnetic phase to the paramagnetic phase. The susceptibility reaches its highest value in the vicinity of this change in the magnetisation and spin overlap, although the peak is not very sharp for the simulations with the J from all data and HC J. Smooth susceptibility is expected as our system is quite small ($N = 84$). The temperature in Metropolis simulations is in units of $1/\sigma_{std}(J)$ where $\sigma_{std}(J)$ is the standard deviation of J.

Critical temperatures T_C were computed as the Metropolis temperature for which the susceptibility was at maximum. The T_C were 0.08 (all data), 0.09 (HC) and 0.07 (AD) in units of $1/\sigma_{std}(J)$. To make the T_C's independent of the specific J used in the simulations, we multiplied them by $\sigma_{std}(J)$ for each respective J. Now, the T_C's are 0.23 (all data), 0.28 (HC) and 0.20 (AD) 10^{-2}. These results should be interpreted in a qualitative

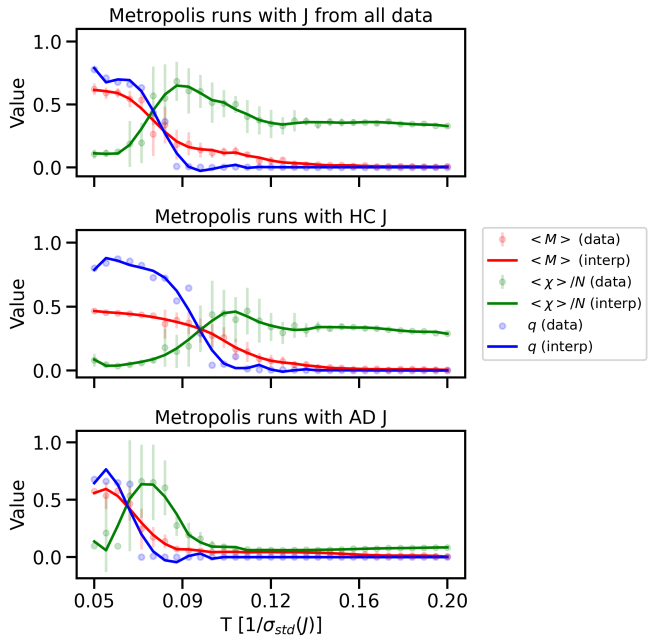

FIG. 19: Average magnetisation $\langle M \rangle$ (red), susceptibility (divided by N) $\langle \chi \rangle / N$ (green), and spin overlap q (blue) as a function of temperature T from Metropolis simulations run with different J. Simulations were run with J extracted from all the data (top), with HC J (middle), and with AD J (bottom). Error bars were plotted based on the standard deviation of the results from the 10 Metropolis realisations. Metropolis T units are $1/\sigma_{std}(J)$ for each respective J.

manner rather than quantitatively. The important result here is that the spin system with the AD J reached the criticality at a lower T than the HC J, with and without the rescaling with respect to J.

IV. DISCUSSION

In this study, we first found the coupling matrix J from the data with the original fMRI-BOLD acquisition parameters. This resulted in very different J and binarised FC matrices across conditions, which was due to the difference in how the data was acquired (sampling rate and length) rather than from patients' conditions. For this reason, we adapted the data to the shortest available acquisition time and with the lowest sampling rate data. This decreased the overall quality and length of the data but eliminated a potential source of bias in the analysis across conditions. The coupling matrices J showed a good correlation with the binarised FC and a lower correlation with the dMRI connectome of each subject (as the matrices were not as sparse as the connectome). Comparing conditions, the only (weak) statistically significant difference was in the homotopic connections. Then, we decided to build average J matrices since the previous results were based on short individual data. This resulted in J matrices, which resembled the dMRI connectomes (more sparse), with a strong homotopic diagonal and good correlation with the binarised FC. The parcels with higher changes in J from HC to AD were, again, mainly homotopic connections. Compared to HCs, in the AD group, the J homotopic connectivity was lower for subcortical areas (insula, thalamus, hippocampus, amygdala, cerebellum) and for the entorhinal, lingual, precuneus, and posterior cingulate areas. The J connectivity was also lower for AD between the middle and superior temporal areas (in both hemispheres). In AD, the J homotopic connectivity of the frontal poles and the connectivity between the rostral middle frontal and superior frontal areas in the LH were higher. Comparing the J matrices by condition, we observed an overall decrease in homotopic connectivity (21%) and the mean connectivity (12%), and more negative connections in AD. These overall changes in J were very dependent on the sparsity value used in the J extraction, apart from homotopic connections, which were consistently higher in HC for both J and binFC. A more thorough optimisation of the sparsity value should also be conducted. In this study, the sparsity parameter was adjusted to balance the correlation of J with both binarised FC and the dMRI-derived connectome and kept constant at 0.1 for both individual and average analyses. Also, the personalised temperatures — obtained by scaling the average J to match individual data — did not differ significantly across conditions. This may be due to the individual data being too short.

Finally, the magnetisation and spin overlap results from the Metropolis simulations suggest that, for all J's, the system transitioned from the ferromagnetic to the paramagnetic state. The peak in susceptibility was not very sharp (especially for the simulations with J from all of the data and HC J), which is expected for a small system ($N = 84$ parcels), as the susceptibility is expected to diverge in an infinite spin lattice, not in a finite system. The results from the simulations also revealed that the spin system simulated with the AD J had a lower critical temperature than the one with the HC J. This means that the AD state is closer to the transition with the paramagnetic (disordered) state, compared to the HC state, and that in the AD spin system, thermal agitation prevails over the parcel-parcel interactions (determined by J) at a lower temperature than HC. Our results can be compared to the work of *Palutla et al. (2023)* [63], who also investigated the distance from the criticality of AD and healthy using spin models with slightly different methods. They detected (second-order) phase transitions by looking at the spatiotemporal correlation lengths over the spin lattice – which are expected to diverge at the critical point – and used them to determine the type of criticality (whether spin-glass or "Ising-like"). They conclude that both conditions seem to be in the spin-glass phases, and that longer relaxation times (in temporal correlations) observed in HC suggest increased proximity to the phase boundary. However, they state that they need more sophisticated order parameters to explain the weak

distinction between spatial correlations across conditions. The analysis of spatiotemporal correlations could be investigated in future work to have additional insights on the criticality analysis. Also, since *Palutla et al. (2023)* [63] found the system to be in the spin-glass phase, it is difficult to compare the results about which condition is closer to the criticality.

This should be interpreted in the framework of the critical brain hypothesis, which suggests that the brain operates near a critical state, where it balances between different dynamical regimes, allowing for optimal responses to internal and external stimuli. This hypothesis proposes that the brain's structural and functional architecture enables it to function effectively at phase transitions, facilitating efficient neural computations and information processing capacities. Recent research has increasingly supported this idea, emphasising the importance of criticality in understanding the healthy brain's dynamics and its ability to transition between cortical states for enhanced cognitive functions [21, 64–70].

One of the main findings of this thesis was the decrease in homotopic connectivity in AD. This agrees with the literature, as several studies claim that the disease is linked to disruptions in the FC of homotopic brain areas, indicating both deterioration of the corpus callosum (the white matter structure connecting the two hemispheres) and changes in inter-hemispheric FC [71–74]. Our results showed a decrease in AD J homotopic connectivity in subcortical areas (including the hippocampus) and posterior cingulate cortex (PCC), and an increase in AD in J connections in temporal areas (in both hemispheres). We did not see a decrease in the hippocampus-PCC connection, and increase in prefrontal-hippocampus and prefrontal-PCC connections (as affirmed by literature [5–10, 75]), but we observed a change in the homotopic connections of these regions. Frontal areas mainly present increased connections in AD, whereas the hippocampus and PCC show decreased connections in AD. Also, a higher percentage of negative connections was found in AD. Negative connections can be interpreted as negative correlations in FC, i.e., as anti-correlated parcels/networks.

This work may be useful in the context of the Neurotwin project (neurotwin.eu), where digital twins of patients are created to design stimulation protocols. A spin-glass digital twin (*spintwin*) can be used to assess the pathology of the subject (as deviating from a normative healthy J) and to design a stimulation treatment that can bring the AD J matrix closer to the healthy one. This would involve representing stimulation effects in the spin-glass model and using the model to generate data and derive a perturbed J matrix, which could then be compared to the normative one. In the clinical trial, the stimulation target comprises the areas of the inferior parietal lobule, prefrontal cortex, temporal lobes, precuneus and hippocampus, based on evidence from previous studies [76–79]. These areas (apart from the inferior parietal lobule) seemed relevant in the changes in J due to condition. As another application, when fMRI-BOLD data is available (with good enough acquisition parameters), the J coupling matrix could be computed and potentially used as a substitute for the dMRI connectome when it is not available. The J matrix is quick to compute and is quite similar to the dMRI-derived brain connectome, but it also captures the homotopic connections and negative (inhibitory) connections, which are missing in dMRI (dMRI can only quantify the presence of fibres at the moment, but not directionality or their nature, excitatory or inhibitory).

One of the main limitations of the study was the length (number of time points), quantity (number of subjects), sampling rate (repetition time), and the homogeneity of these parameters across conditions of the fMRI-BOLD data. *Ezaki et al. (2017)* [20] state that the accuracy of the pseudo-likelihood maximisation (used to extract J) is proportional to $t_{max}/2^N$. Their argument was based on the probability that each of the 2^N possible activity patterns appears compared between the empirical data and the estimated spin model. This suggests that the accuracy for the individual J was low due to the limited data length to accommodate for $N = 84$ parcels. In our study, the sparsity parameter was introduced to be able to work with shorter data by forcing the matrix to be sparse. With sparsity, we control the noise in the estimation, but we "bias" the result (to lower sparsity), which may be correct or not. Hence, further work should assess the validity of this prior, and the minimum data length required to get a robust J. In this study, the criteria to accept the J matrix was based on the correlation with the original binarised FC.

A limitation regarding the Metropolis simulations to determine the critical temperature for each J, was that we did not build a theoretical phase diagram for J based on its mean μ and standard deviation σ_{std} as *Ezaki et al. (2020)* [21] did in their study. They did this by defining $J_{ij} = (\hat{J}_{ij} - \hat{\mu})\frac{\sigma_{std}}{\hat{\sigma}_{std}} + \mu$ (where $\hat{\mu}$ and $\hat{\sigma}_{std}$ are determined from the data) and then exploring the phase space (with the calculation of the magnetisation, susceptibility etc.) varying σ_{std} and μ (in their work $T = 1$ always). Using higher resolution and longer data, sparser J matrices can be obtained (as we did with the original AD data, see Figure 20), and each subject could be located on the phase diagram simply by using their J mean and standard deviation. This would give a more complete picture of the position of each J in the phase diagram. In *Ezaki et al. (2020)* [21] they state that subjects with lower $\sigma_{std}(J)$ (at a fixed J mean) are closer to the ferromagnetic-paramagnetic phase transition, whereas the paramagnetic-spin-glass transition happens for higher $\sigma_{std}(J)$ (at a fixed J mean). In our study, even after downsampling, we found that there was a statistically significant ($p = 0.0039$) difference between the standard deviation of J, $\sigma_{std}(J)$, across conditions, with the HC $\sigma_{std}(J)$ being higher than in AD. The same trend was observed for their means, although this was not statistically significant. The results depended on the spar-

sity value (set to 0.1 in the whole study), which affected the standard deviation of J (higher sparsity gives lower standard deviation) — which changes the critical temperature. However, AD always had a lower critical temperature than HC.

V. CONCLUSIONS

In the first part of this thesis, pseudo-likelihood maximisation based on formalism from the Sherrington-Kirkpatrick spin-glass model was used to extract coupling matrices J from fMRI-BOLD data acquired from elderly subjects diagnosed with AD and healthy controls. Comparing the J from the AD and healthy subjects, the main and most robust result was the decrease in homotopic connectivity in the AD J ($p = 0.0496$ with individual subject data), which agrees with other studies on the inter-hemispheric and homotopic connectivity disruption in AD. Also, the difference between the HC and AD J's standard deviation values was statistically significant ($p = 0.0039$). Further statistical analysis, e.g., bootstrapping and leave-one-out methods, may be employed in future work to assess the robustness of these results. Also, these results depended on the sparsity value, apart from homotopic connections which were consistently higher in HC for both J and binFC. A more thorough optimisation of the sparsity value should also be conducted. In this study, the value was adjusted to balance the correlation of J with both binarised FC and the dMRI-derived connectome. Additionally, some of the brain areas with the highest change in J between HC and AD (subcortical, frontal and temporal areas) seemed relevant in the literature on FC changes in AD.

In the second part of this thesis, the spin-glass systems (defined by the average J's specific to the condition) were simulated with the Metropolis algorithm at different system temperatures to assess the presence of phase transitions, the type of criticality and the critical temperature, for every condition. The main result was that the simulations of the spin lattice using the AD J showed a lower critical temperature than those with the healthy J. We hypothesise that both the AD and HC spin lattices underwent a phase transition from the ferromagnetic to the paramagnetic states (due to the changes in magnetisation, spin overlap and susceptibility). This may mean that the AD state is closer to the transition with the paramagnetic (disordered) state than the HC state, with weaker connections between parcels. However, a more thorough investigation of the phase space of J should be carried out in future work to shed more light on the criticality findings.

Generally, the J coupling matrix seems to capture structural features and homotopic connections, and it could be used as a synthetic brain connectome when dMRI data is unavailable. The data length (after downsampling and trimming) influenced the results when analysing individual datasets. The fit of the coupling matrix improved when constructing an average model that combined all data by condition. However, longer data sequences are necessary for the pseudo-likelihood approximation to be valid, as the accuracy is proportional to $t_{max}/2^N$ [20].

Future work includes conducting a criticality analysis based on longer individual data by using the Metropolis algorithm, along with implementing parallel tempering. Additionally, we could test the pipeline with other HC fMRI-BOLD data, particularly those with acquisition parameters similar to the AD data. It is also important to compare pre- and post-stimulation data from the Neurotwin clinical trial to determine if post-stimulation features shift towards those of a healthy state. Another key step involves comparing the J coupling matrix to positron emission tomography (PET) maps once they become available for AD patients. PET data is also very valuable in AD as it shows the accumulation of proteins (amyloid beta and tau) associated with the presence of the disease [80]. It may be interesting to check the correlation between J and the PET maps, as the protein agglomerations could potentially disrupt connectivity between brain regions. To improve the statistical analysis, we should consider using data from more subjects (this was limited due to time constraints), bootstrapping methods, and repeating the analysis leaving out part of the sample. Network analysis on J could also be interesting. This would involve assigning parcels to main brain networks to check the overall difference from HC to AD in these networks. Finally, we plan to examine structural changes from MRI, such as parcel size changes due to atrophy and check how this affects the percentage of functional signals in a brain region.

Appendix A: fMRI-BOLD acquisition parameters

The fMRI-BOLD scan parameters, specifically repetition time and number of time points, are shown for each subject in Table II.

ID	Repetition Time (s)	Time points
AD_7	1.0	487
AD_4	1.0	487
AD_8	1.0	487
AD_9	1.0	487
AD_10	1.0	487
AD_14	1.0	487
AD_15	1.0	487
AD_6	1.0	487
AD_3	1.0	487
AD_16	1.0	487
AD_18	1.0	487
AD_25	1.0	487
AD_29	1.0	487
AD_30	1.0	487
AD_31	1.0	487
AD_1	1.0	487
AD_2	1.0	487
HC_58	3.0	196
HC_9	3.0	196
HC_59	3.0	199
HC_63	3.0	196
HC_13	3.0	139
HC_14	3.0	139
HC_4	3.0	139
HC_18	0.6	975
HC_62	3.0	199
HC_17	0.6	975
HC_24	3.0	196
HC_60	3.0	196
HC_26	3.0	199
HC_3	3.0	139
HC_61	3.0	196

TABLE II: fMRI scan parameters for all subjects.

Appendix B: Desikan84 Parcellation Scheme

Table B shows the Desikan84 parcellation scheme. 'LH' and 'RH' stand respectively for left and right hemispheres, and 'Idx' is the parcel index.

Idx	LH Parcel	Idx	RH Parcel
0	LH Banks STS	42	RH Cerebellum
1	LH Caudal Anterior Cingulate	43	RH Accumbens
2	LH Caudal Middle Frontal	44	RH Amygdala
3	LH Cuneus	45	RH Hippocampus
4	LH Entorhinal	46	RH Pallidum
5	LH Fusiform	47	RH Putamen
6	LH Inferior Parietal	48	RH Caudate
7	LH Inferior Temporal	49	RH Thalamus
8	LH Isthmus Cingulate	50	RH Insula
9	LH Lateral Occipital	51	RH Transverse Temporal
10	LH Lateral Orbito Frontal	52	RH Temporal Pole
11	LH Lingual	53	RH Frontal Pole
12	LH Medial Orbito Frontal	54	RH Supra Marginal
13	LH Middle Temporal	55	RH Superior Temporal
14	LH Parahippocampal	56	RH Superior Parietal
15	LH Paracentral	57	RH Superior Frontal
16	LH Pars Opercularis	58	RH Rostral Middle Frontal
17	LH Pars Orbitalis	59	RH Rostral Anterior Cingulate
18	LH Pars Triangularis	60	RH Precuneus
19	LH Pericalcarine	61	RH Precentral
20	LH Postcentral	62	RH Posterior Cingulate
21	LH Posterior Cingulate	63	RH Postcentral
22	LH Precentral	64	RH Pericalcarine
23	LH Precuneus	65	RH Pars Triangularis
24	LH Rostral Anterior Cingulate	66	RH Pars Orbitalis
25	LH Rostral Middle Frontal	67	RH Pars Opercularis
26	LH Superior Frontal	68	RH Paracentral
27	LH Superior Parietal	69	RH Parahippocampal
28	LH Superior Temporal	70	RH Middle Temporal
29	LH Supra Marginal	71	RH Medial Orbito Frontal
30	LH Frontal Pole	72	RH Lingual
31	LH Temporal Pole	73	RH Lateral Orbito Frontal
32	LH Transverse Temporal	74	RH Lateral Occipital
33	LH Insula	75	RH Isthmus Cingulate
34	LH Thalamus	76	RH Inferior Temporal
35	LH Caudate	77	RH Inferior Parietal
36	LH Putamen	78	RH Fusiform
37	LH Pallidum	79	RH Entorhinal
38	LH Hippocampus	80	RH Cuneus
39	LH Amygdala	81	RH Caudal Middle Frontal
40	LH Accumbens	82	RH Caudal Anterior Cingulate
41	LH Cerebellum	83	RH Banks STS

TABLE III: Desikan84 parcellation scheme with indices.

Appendix C: J coupling matrices for data with original fMRI-BOLD scan parameters

Here are the J coupling matrices (upper triangle) and binarised FC (lower triangle) for AD (Figure 20) and HC subjects (Figure 21), from the data with original scan parameters.

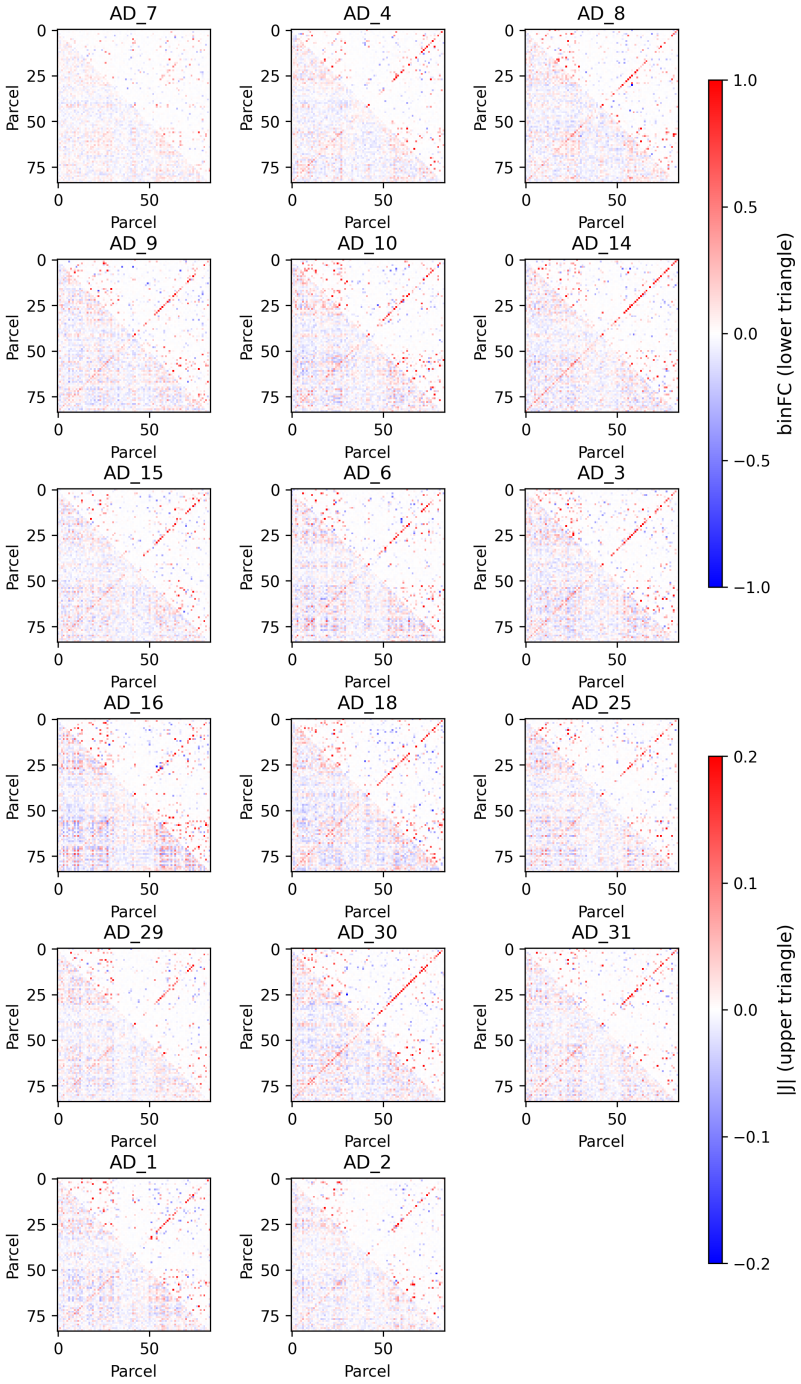

FIG. 20: J coupling matrices (upper triangle) and binarised FC (lower triangle) for individual original AD data.

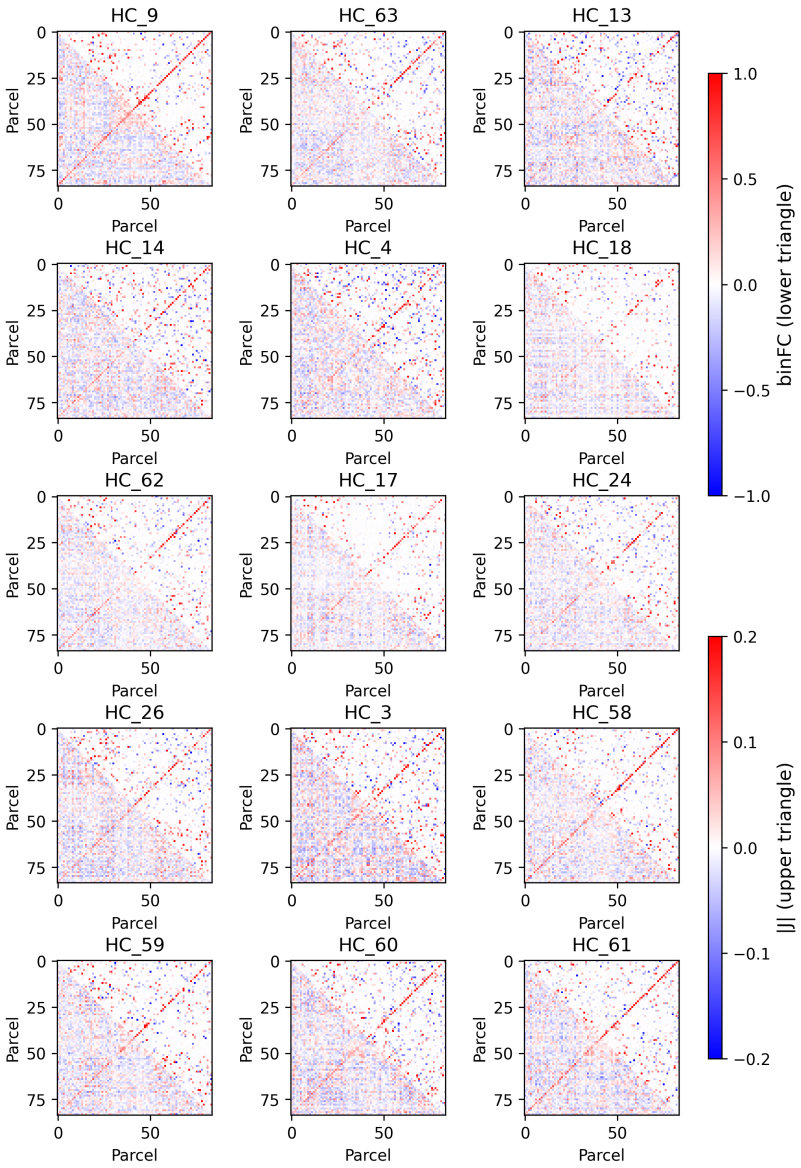

FIG. 21: J coupling matrices (upper triangle) and binarised FC (lower triangle) for individual original HC data.

Appendix D: J coupling matrices for down-sampled and truncated data

Here are the J coupling matrices (upper triangle) and binarised FC (lower triangle) for AD (Figure 22) and HC subjects (Figure 23), from the down-sampled and cut data.

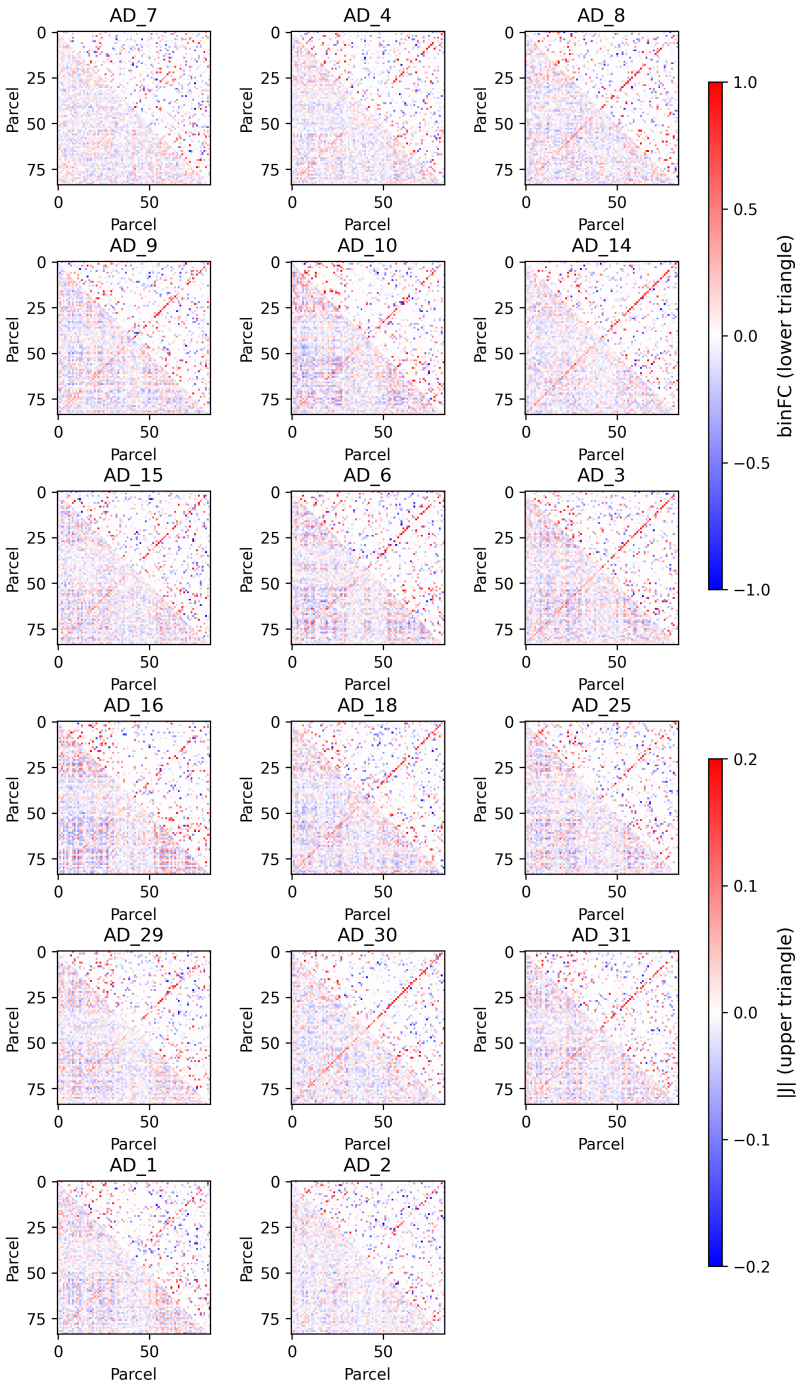

FIG. 22: J coupling matrices (upper triangle) and binarised FC (lower triangle) for individual down-sampled AD data.

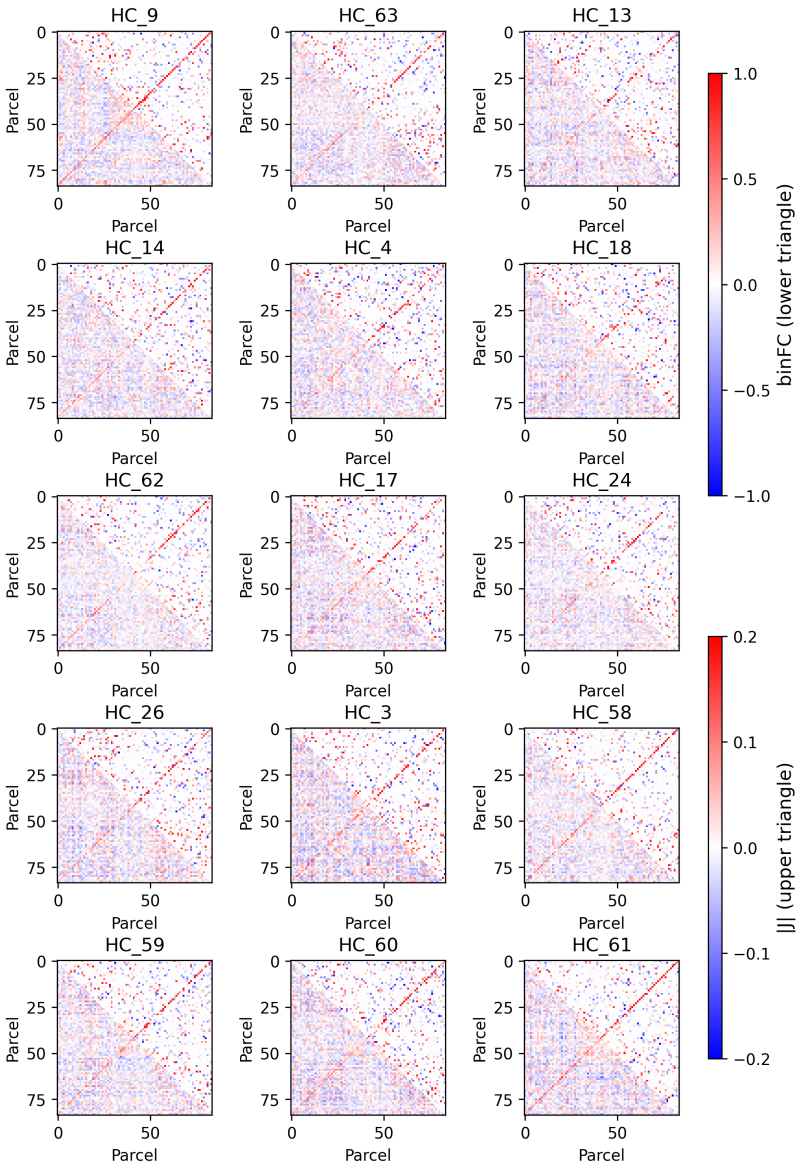

FIG. 23: J coupling matrices (upper triangle) and binarised FC (lower triangle) for individual down-sampled HC data.

Appendix E: Average J and binarised FC difference from HC to AD with brain parcel names

Figures 24 and 25 show respectively the relative difference in J and the binarised FC from HC to AD. Parcels with a change higher than 70% of maximum change (in absolute value) were highlighted and labelled.

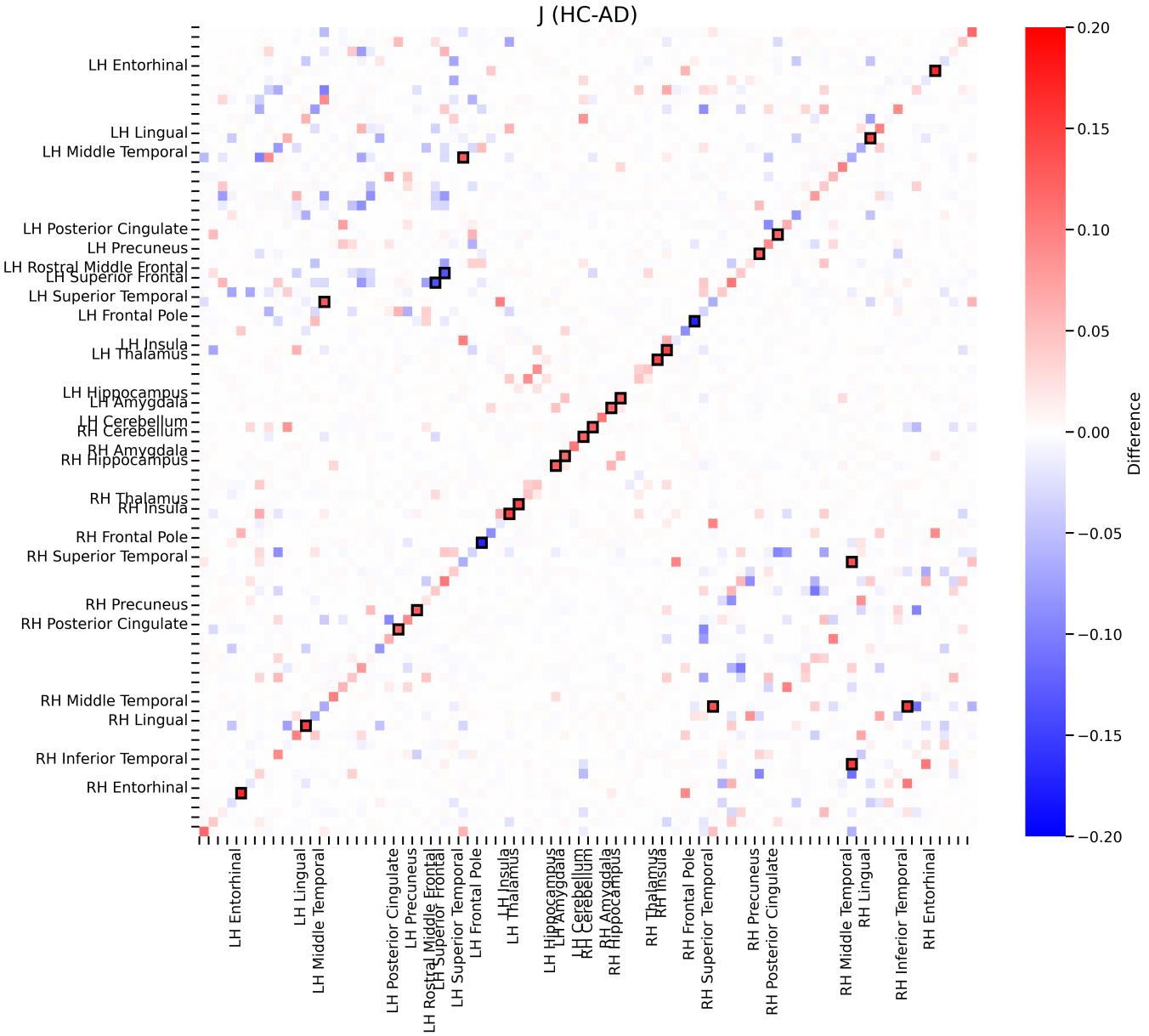

FIG. 24: Difference HC - AD in J coupling matrices. Brain parcels were highlighted if the change was higher than 70% of maximum change (in absolute value).

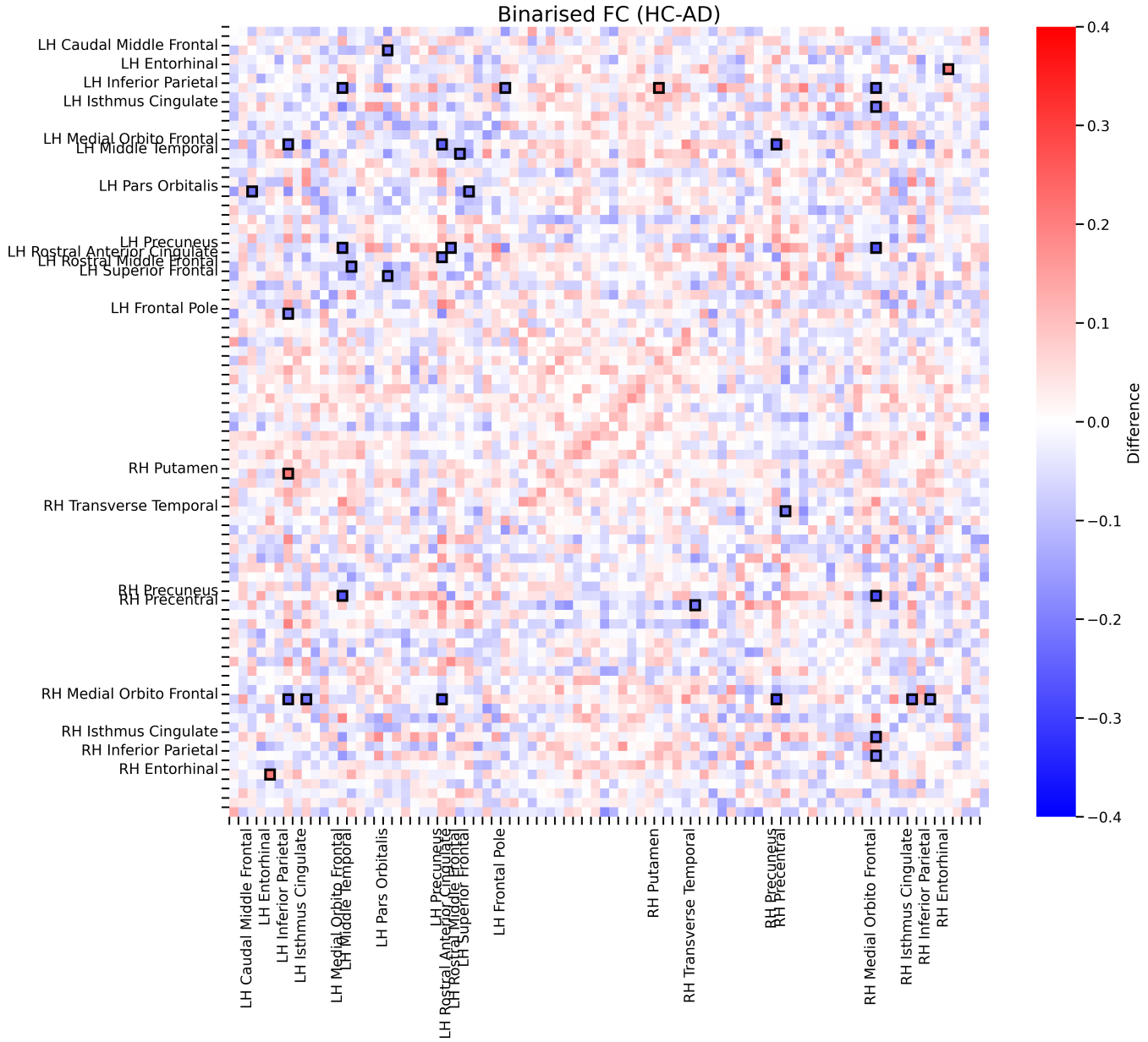

FIG. 25: Difference HC - AD in binarised FC. Brain parcels were highlighted if the change was higher than 70% of maximum change (in absolute value).

ACKNOWLEDGMENTS

This project has received funding from the European Union's Horizon 2020 research and innovation programme under grant agreement No 101017716 (Neurotwin project, neurotwin.eu). I would like to thank my advisors for their guidance and insightful conversations, and the Neuroelectrics team for their support and help processing the data. I would like to thank the Neurotwin project for sharing the clinical trial data and for their financial support.

Dedico questa tesi a Nonno Carlo che sarebbe stato immensamente orgoglioso di celebrare questo traguardo con me. Ringrazio tutta la mia famiglia per avermi sempre supportato, incoraggiato a perseguire i miei obiettivi, aiutato a costruire radici forti e insegnato valori come la determinazione, l'empatia e l'onestà.

Finalmente, gostaria de agradecer à minha escola de capoeira por estar sempre ao meu lado nos momentos difíceis, recarregando-me com energia positiva para enfrentar os desafios.

[1] P. Scheltens, B. De Strooper, M. Kivipelto, H. Holstege, G. Chételat, C. E. Teunissen, J. Cummings, and W. M. van der Flier, Alzheimer's disease, Lancet **397**, 1577 (2021).

[2] H. Geerts, P. A. Dacks, V. Devanarayan, M. Haas, Z. S. Khachaturian, M. F. Gordon, S. Maudsley, K. Romero, D. Stephenson, and B. H. M. I. (BHMI), Big data to smart data in alzheimer's disease: The brain health modeling initiative to foster actionable knowledge, Alzheimer's Dementia **12**, 1014 (2016).

[3] O. J. Arthurs and S. Boniface, How well do we understand the neural origins of the fmri bold signal?, Trends in Neurosciences **25**, 27 (2002).

[4] M. P. van den Heuvel and H. E. Hulshoff Pol, Exploring the brain network: A review on resting-state fmri functional connectivity, European Neuropsychopharmacology **20**, 519 (2010).

[5] L. Wang, Y.-F. Zang, Y. He, M. Liang, X. Zhang, L. Tian, T. Wu, T. Jiang, and K. Li, Changes in hippocampal connectivity in the early stages of alzheimer's disease: evidence from resting state fmri, NeuroImage **31**, 496 (2006).

[6] G. Allen, H. Barnard, R. McColl, A. L. Hester, J. A. Fields, M. F. Weiner, W. K. Ringe, A. M. Lipton, M. Brooker, E. McDonald, C. D. Rubin, and C. M. Cullum, Reduced hippocampal functional connectivity in alzheimer disease, Archives of Neurology **64**, 1482 (2007).

[7] H.-Y. Zhang, S.-J. Wang, J. Xing, B. Liu, Z.-L. Ma, M. Yang, Z.-J. Zhang, and G.-J. Teng, Detection of pcc functional connectivity characteristics in resting-state fmri in mild alzheimer's disease, Behavioural Brain Research **197**, 103 (2009).

[8] J. P. Bai, R. Bell, S. Buckman, G. J. Burckart, H. G. Eichler, K. C. Fang, F. M. Goodsaid, W. J. Jusko, L. L. Lesko, B. Meibohm, S. D. Patterson, O. Puig, J. B. Smerage, B. J. Snider, J. A. Wagner, J. Wang, M. K. Walton, and R. Weiner, Translational biomarkers: from preclinical to clinical a report of 2009 aaps/accp biomarker workshop, AAPS Journal **13**, 274 (2011).

[9] B. C. Dickerson, D. H. Salat, J. F. Bates, M. Atiya, R. J. Killiany, D. N. Greve, A. M. Dale, C. E. Stern, D. Blacker, M. S. Albert, and R. A. Sperling, Medial temporal lobe function and structure in mild cognitive impairment, Annals of Neurology **56**, 27 (2004).

[10] E. J. Sanz-Arigita, M. M. Schoonheim, J. S. Damoiseaux, S. A. R. B. Rombouts, E. Maris, F. Barkhof, P. Scheltens, and C. J. Stam, Loss of 'small-world' networks in alzheimer's disease: graph analysis of fmri resting-state functional connectivity, PLoS One **5**, e13788 (2010).

[11] M. Filippi and F. Agosta, Structural and functional network connectivity breakdown in alzheimer's disease studied with magnetic resonance imaging techniques, Journal of Alzheimer's Disease **24**, 455 (2011).

[12] J. Cabral, H. Luckhoo, M. Woolrich, M. Joensson, H. Mohseni, A. Baker, M. L. Kringelbach, and G. Deco, Exploring mechanisms of spontaneous functional connectivity in MEG: How delayed network interactions lead to structured amplitude envelopes of band-pass filtered oscillations, NeuroImage **90**, 423 (2014).

[13] Nuclear magnetic resonance imaging in medicine and biology.

[14] G. B. Frisoni, N. C. Fox, C. R. Jack, P. Scheltens, and P. M. Thompson, The clinical use of structural mri in alzheimer disease, Nature Reviews Neurology **6**, 67 (2010).

[15] D. Le Bihan, Looking into the functional architecture of the brain with diffusion mri, Nature Reviews Neuroscience **4**, 469 (2003).

[16] D. R. Chialvo, Critical brain networks, Physica A **340**, 756 (2004).

[17] D. R. Chialvo, enEmergent complex neural dynamics, Nat. Phys. **6**, 744 (2010).

[18] T. Das, P. Abeyasinghe, J. S. Crone, A. Sosnowski, S. Laureys, A. M. Owen, and A. Soddu, Highlighting the structure-function relationship of the brain with the ising model and graph theory, BioMed Research International (2014).

[19] L. Cocchi, L. L. Gollo, A. Zalesky, and M. Breakspear, enCriticality in the brain: A synthesis of neurobiology, models and cognition, Prog. Neurobiol. **158**, 132 (2017).

[20] T. Ezaki, T. Watanabe, M. Ohzeki, and N. Masuda, Energy landscape analysis of neuroimaging data, Philos Trans R Soc A **375** (2017).

[21] T. Ezaki, E. Fonseca Dos Reis, T. Watanabe, M. Sakaki, and N. Masuda, enCloser to critical resting-state neural dynamics in individuals with higher fluid intelligence, Commun. Biol. **3**, 52 (2020).

[22] D. Fraiman, P. Balenzuela, J. Foss, and D. R. Chialvo, enIsing-like dynamics in large-scale functional brain networks, Phys. Rev. E Stat. Nonlin. Soft Matter Phys. **79**, 061922 (2009).

[23] E. Niebur and D. Plenz, eds., en*Criticality in Neural Systems*, Annual Reviews of Nonlinear Dynamics and Complexity (VCH) (Wiley-VCH Verlag, Weinheim, Germany,

2014).
[24] S. Yu, H. Yang, O. Shriki, and D. Plenz, enUniversal organization of resting brain activity at the thermodynamic critical point, Front. Syst. Neurosci. **7**, 42 (2013).
[25] R. Lewin, en*Complexity*, 2nd ed. (University of Chicago Press, Chicago, IL, 1992).
[26] N. Goldenfeld, *Lectures on Phase Transitions and the Renormalization Group* (Addison Wesley, London, England, 1991).
[27] W. L. Shew and D. Plenz, enThe functional benefits of criticality in the cortex, Neuroscientist **19**, 88 (2013).
[28] P. A. M. Mediano and M. Shanahan, Balanced information storage and transfer in modular spiking neural networks, arxiv (2017), arXiv:1708.04392 [q-bio.NC].
[29] E. Erten, J. Lizier, M. Piraveenan, and M. Prokopenko, Criticality and information dynamics in epidemiological models, Entropy (Basel) **19**, 194 (2017).
[30] M. Li, Y. Han, M. J. Aburn, M. Breakspear, R. A. Poldrack, J. M. Shine, and J. T. Lizier, Transitions in information processing dynamics at the whole-brain network level are driven by alterations in neural gain, PLOS Computational Biology **15**, 1 (2019).
[31] P. A. M. Mediano, F. E. Rosas, J. C. Farah, M. Shanahan, D. Bor, and A. B. Barrett, Integrated information as a common signature of dynamical and information-processing complexity, Chaos **32**, 13115 (2022).
[32] G. Deco and V. K. Jirsa, enOngoing cortical activity at rest: criticality, multistability, and ghost attractors, J. Neurosci. **32**, 3366 (2012).
[33] G. Deco, V. Jirsa, A. R. McIntosh, O. Sporns, and R. Kötter, Key role of coupling, delay, and noise in resting brain fluctuations, Proceedings of the National Academy of Sciences **106**, 10302 (2009).
[34] F. Cieri, X. Zhuang, J. Z. K. Caldwell, and D. Cordes, Brain entropy during aging through a free energy principle approach, Frontiers in Human Neuroscience **15**, 139 (2021).
[35] E. Tagliazucchi, P. Balenzuela, D. Fraiman, and D. R. Chialvo, Criticality in large-scale brain FMRI dynamics unveiled by a novel point process analysis, Front. Physiol. **3**, 15 (2012).
[36] A. Haimovici, E. Tagliazucchi, P. Balenzuela, and D. R. Chialvo, enBrain organization into resting state networks emerges at criticality on a model of the human connectome, Phys. Rev. Lett. **110**, 178101 (2013).
[37] D. Marinazzo, M. Pellicoro, G. Wu, L. Angelini, J. M. Cortés, and S. Stramaglia, enInformation transfer and criticality in the ising model on the human connectome, PLoS One **9**, e93616 (2014).
[38] F. Hancock, F. Rosas, P. Mediano, A. Luppi, J. Cabral, O. Dipasquale, and F. Turkheim, May the 4c's be with you: An overview of complexity-inspired frameworks for analyzing resting-state neuroimaging data (2022).
[39] H. J. Jensen, *Self-Organized Criticality: Emergent Complex Behavior in Physical and Biological Systems*, Cambridge Lecture Notes in Physics (Cambridge University Press, 1998).
[40] G. Pruessner, *Self-Organised Criticality* (Cambridge University Press, Cambridge, England, 2012).
[41] K. Christensen and N. R. Moloney, *Complexity and criticality* (Imperial College Press, London, England, 2005).
[42] M. W. Weiner, D. P. Veitch, P. S. Aisen, L. A. Beckett, N. J. Cairns, R. C. Green, D. Harvey, C. R. Jack, W. Jagust, J. C. Morris, R. C. Petersen, J. Salazar, A. J. Saykin, L. M. Shaw, A. W. Toga, and J. Q. Trojanowski, The alzheimer's disease neuroimaging initiative 3: Continued innovation for clinical trial improvement, Alzheimer's Dementia **13**, 561 (2017).
[43] G. Ruffini, G. Damiani, D. Lozano-Soldevilla, N. Deco, F. E. Rosas, N. A. Kiani, A. Ponce-Alvarez, M. L. Kringelbach, R. Carhart-Harris, and G. Deco, Lsd-induced increase of ising temperature and algorithmic complexity of brain dynamics, PLoS Comput Biol **19**, e1010811 (2023).
[44] O. Esteban, C. J. Markiewicz, R. W. Blair, C. A. Moodie, A. I. Isik, A. Erramuzpe, J. D. Kent, M. Goncalves, E. DuPre, M. Snyder, *et al.*, fmriprep: a robust preprocessing pipeline for functional mri, Nature Methods **16**, 111 (2019).
[45] B. Fischl, Freesurfer, Neuroimage **62**, 774 (2012).
[46] B. B. Avants, N. J. Tustison, G. Song, P. A. Cook, A. Klein, and J. C. Gee, The insight toolkit image registration framework, Frontiers in Neuroinformatics **5**, 13 (2011).
[47] R. S. Desikan, F. Ségonne, B. Fischl, B. T. Quinn, B. C. Dickerson, D. Blacker, R. L. Buckner, A. M. Dale, R. P. Maguire, B. T. Hyman, M. S. Albert, and R. J. Killiany, An automated labeling system for subdividing the human cerebral cortex on mri scans into gyral based regions of interest, NeuroImage **31**, 968 (2006).
[48] J. Tournier, F. Calamante, and A. Connelly, Mrtrix: Diffusion tractography in crossing fiber regions, International Journal of Imaging Systems and Technology **22**, 53 (2012).
[49] E. Jaynes, Information theory and statistical mechanics, Physical Review **106**, 620 (1957).
[50] E. Jaynes, *Probability theory - the logic of science* (Cambridge, 2003).
[51] E. Schneidman, M. J. B. II, R. Segev, and W. Bialek, Weak pairwise correlations imply strongly correlated network states in a neural population, Nature **440**, 1007 (2006).
[52] A. M. Turing, enI.—computing machinery and intelligence, Mind **LIX**, 433 (1950).
[53] P. Bak, C. Tang, and K. Wiesenfeld, enSelf-organized criticality: An explanation of the 1/f noise, Phys. Rev. Lett. **59**, 381 (1987).
[54] J. J. Hopfield, Neural networks and physical systems with emergent collective computational abilities, PNAS **79**, 2554 (1982).
[55] V. Priesemann, M. Wibral, M. Valderrama, R. Pröpper, M. Le Van Quyen, T. Geisel, J. Triesch, D. Nikolić, and M. H. J. Munk, enSpike avalanches in vivo suggest a driven, slightly subcritical brain state, Front. Syst. Neurosci. **8**, 108 (2014).
[56] R. Carhart-Harris, The entropic brain — revisited, Neuropharmacology **142** (2018).
[57] D. Sherrington and S. Kirkpatrick, Solvable model of a spin-glass, Phys. Rev. Lett. **35**, 1792 (1975).
[58] A. P. Young, Numerical simulations of spin glasses: Methods and some recent results, in *Computer Simulations in Condensed Matter Systems: From Materials to Chemical Biology Volume 2*, Lecture Notes in Physics, Vol. 704, edited by M. Ferrario, G. Ciccotti, and K. Binder (Springer, 2006) pp. 31–66.
[59] J. Besag, Statistical analysis of non-lattice data, J. R. Stat. Soc. D **25**, 179 (1975).

[60] R. Pathria and P. D. Beale, *Statistical Mechanics* (Elsevier Ltd, 2011).
[61] E. Ibarra-García-Padilla, C. G. Malanche-Flores, and F. J. Poveda-Cuevas, The hobbyhorse of magnetic systems: the ising model, Eur. J. Phys. **37**, 065103 (2016).
[62] S. Burkhardt, *Efficiency of Parallel Tempering for Ising Systems*, Masters theses, University of Massachusetts Amherst (2010), accessed: 2024-06-26.
[63] A. Palutla, S. Seth, S. S. Ashwin, and M. Krishnan, Criticality in alzheimer's and healthy brains: insights from phase-ordering, Cognitive Neurodynamics (2023).
[64] J. Shi, K. Kirihara, M. Tada, M. Fujioka, K. Usui, D. Koshiyama, T. Araki, L. Chen, K. Kasai, and K. Aihara, Criticality in the healthy brain, Frontiers in Network Physiology 10.3389/fnetp.2021.755685 (2022).
[65] T. Groß, Not one, but many critical states: A dynamical systems perspective, Frontiers in Neural Circuits 10.3389/fncir.2021.614268 (2021).
[66] R. P. Rocha, L. Koçillari, S. Suweis, M. D. F. Grazia, M. T. de Schotten, M. Zorzi, and M. Corbetta, Recovery of neural dynamics criticality in personalized whole brain models of stroke 10.1101/2020.12.17.423349 (2020).
[67] R. P. Rocha, L. Koçillari, S. Suweis, M. D. F. Grazia, M. T. de Schotten, M. Zorzi, and M. Corbetta, Recovery of neural dynamics criticality in personalized whole-brain models of stroke, Nature Communications 10.1038/s41467-022-30892-6 (2022).
[68] J. Hesse and T. Groß, Self-organized criticality as a fundamental property of neural systems, Frontiers in Systems Neuroscience 10.3389/fnsys.2014.00166 (2014).
[69] J. M. Beggs and N. M. Timme, Being critical of criticality in the brain, Frontiers in Physiology 10.3389/fphys.2012.00163 (2012).
[70] J. M. Beggs, Addressing skepticism of the critical brain hypothesis, Frontiers in Computational Neuroscience 10.3389/fncom.2022.703865 (2022).
[71] Y. Qiu, S. Liu, S. Hilal, Y. M. Loke, M. K. Ikram, X. Xu, B. Y. Tan, N. Venketasubramanian, C. Chen, and J. Zhou, Inter-hemispheric functional dysconnectivity mediates the association of corpus callosum degeneration with memory impairment in ad and amnestic mci, Scientific Reports 10.1038/srep32573 (2016).
[72] Z. Wang, J. Wang, H. Zhang, R. Mchugh, X. Sun, K. Li, and Q. X. Yang, Interhemispheric functional and structural disconnection in alzheimer's disease: A combined resting-state fmri and dti study, PLOS ONE **10**, 1 (2015).
[73] S. Chen, H. Wu, Y. Song, H. Ge, Z. Yan, C. Xue, W. Qi, Q. Yuan, X. Lin, and J. Chen, Altered structural and functional homotopic connectivity associated with the progression from mild cognitive impairment to alzheimer's disease, Psychiatry Research **319**, 115000 (2023).
[74] E. Y. W. Cheung, Y. F. Shea, P. K. C. Chiu, J. S. K. Kwan, and H. K. F. Mak, Diagnostic efficacy of voxel-mirrored homotopic connectivity in vascular dementia as compared to alzheimer's related neurodegenerative diseases—a resting state fmri study, Life **11**, 10.3390/life11101108 (2021).
[75] F. Agosta, M. Pievani, C. Geroldi, M. Copetti, G. B. Frisoni, and M. Filippi, Resting state fmri in alzheimer's disease: beyond the default mode network, Neurobiology of Aging **33**, 1564 (2012).
[76] S. Grover, W. Wen, V. Viswanathan, C. T. Gill, and R. M. G. Reinhart, Long-lasting, dissociable improvements in working memory and long-term memory in older adults with repetitive neuromodulation, Nature Neuroscience **25**, 1237 (2022).
[77] G. Sprugnoli, F. Munsch, D. Cappon, R. Paciorek, J. Macone, A. Connor, G. El Fakhri, R. Salvador, G. Ruffini, K. Donohoe, M. M. Shafi, D. Press, D. C. Alsop, A. Pascual-Leone, and E. Santarnecchi, Impact of multisession 40hz tacs on hippocampal perfusion in patients with alzheimer's disease, Alzheimer's Research Therapy **13**, 203 (2021).
[78] G. Koch, E. P. Casula, S. Bonnì, I. Borghi, M. Assogna, M. Minei, M. C. Pellicciari, C. Motta, A. D'Acunto, F. Porrazzini, M. Maiella, C. Ferrari, C. Caltagirone, E. Santarnecchi, M. Bozzali, and A. Martorana, Precuneus magnetic stimulation for Alzheimer's disease: a randomized, sham-controlled trial, Brain **145**, 3776 (2022), https://academic.oup.com/brain/article-pdf/145/11/3776/47187808/awac285.pdf.
[79] M. Vyhnálek, H. Marková, J. Laczó, R. De Beni, and S. Di Nuovo, Assessment of memory impairment in early diagnosis of alzheimer's disease, Current Alzheimer Research **16**, 975 (2019).
[80] A. Nordberg, J. O. Rinne, A. Kadir, and B. Långström, The use of pet in alzheimer disease, Nature Reviews Neurology **6**, 78 (2010).